metals

MDPI

Article

Phase Transitions and Structural Evolution of Manganese Ores During High-Temperature Treatment

Ruslan Z. Safarov [1], Yerlan A. Baikenov [1,*], Assemgul K. Zhandildenova [1,*], Eldar E. Kopishev [1], Ruslan M. Kamatov [2], Jumat B. Kargin [3], H. Sanchez Cornejo [4], Crispin H. W. Barnes [5] and Luis De Los Santos Valladares [5,6]

1 Department of Chemistry, Faculty of Natural Sciences, L.N. Gumilyov Eurasian National University, Astana 010008, Kazakhstan; safarov_rz@enu.kz (R.Z.S.); kopishev_eye@enu.kz (E.E.K.)
2 Department of Science, L.N. Gumilyov Eurasian National University, Astana 010008, Kazakhstan; kamatov_rm@enu.kz
3 Department of Technical Physics, Faculty of Physics and Technical Sciences, L.N. Gumilyov Eurasian National University, Astana 010008, Kazakhstan; kargin_db@enu.kz
4 Laboratorio de Cerámicos y Nanomateriales, Facultad de Ciencias Físicas, Universidad Nacional Mayor de San Marcos, Ap. Postal 14-0149, Lima 15081, Peru; henry.sanchez@unmsm.edu.pe
5 Cavendish Laboratory, Department of Physics, University of Cambridge, J.J. Thomson Ave., Cambridge CB3 0HE, UK; chwb101@cam.ac.uk (C.H.W.B.); ld301@cam.ac.uk (L.D.L.S.V.)
6 Programa de Pós-Graduação em Ciências de Materiais, Centro de Ciências Exatas e da Natureza, Universidade Federal de Pernambuco, Recife 50670-901, Brazil
* Correspondence: baikenov_yea_1@enu.kz (Y.A.B.); astana@cse.kz (A.K.Z.)

Abstract: The aim of this research is to investigate the phase composition and structural peculiarities of complex metamorphic manganese ores from Central Kazakhstan before and after sintering in the temperature range of 600–1200 °C in an air atmosphere. X-ray diffraction, X-ray fluorescence, scanning electron microscopy, and optical microscopy were used to analyze changes in elemental and phase composition. In their initial state, according to XRF analysis, the Bogach ore was manganese-rich, with a manganese content of 60.77 wt.%, while the Zhaksy ore contained manganese (44.88 wt.%), silicon (20.85 wt.%), and iron (6.14 wt.%) as its main components. In the Bogach ore samples, manganese content increased from 60.77% to 65.7% as the sintering temperature rose to 1100 °C, while the hausmannite phase (Mn_3O_4) emerged as the dominant phase, comprising 95.77% of the crystalline component at 1200 °C. Conversely, the Zhaksy ore samples displayed a sharp increase in braunite-phase ($Mn_7O_{12}Si$) content, reaching 83.81% at 1100 °C, alongside significant quartz amorphization. The degree of crystallinity in Bogach ore peaked at 56.2% at 900 °C but declined at higher temperatures due to amorphous phase formation. A surface morphology analysis revealed the transformation of dense, non-uniform particles into porous, granular structures with pronounced recrystallization as the temperature increased. In the Bogach samples, sintering at 900 °C resulted in elongated, needle-like crystalline formations, while at 1200 °C, tetragonal crystals of hausmannite dominated, indicating significant grain growth and recrystallization. For Zhaksy samples, sintering at 1100 °C led to a porous morphology with interconnected grains and microvoids, reflecting enhanced braunite crystallization and quartz amorphization. These findings provide quantitative insights into optimizing manganese oxide phases for industrial applications, such as catalysts and pigments, and emphasize the impact of thermal treatment on phase stability and structural properties. This research contributes to the development of efficient processing technologies for medium-grade manganese ores, aligning with Kazakhstan's strategic goals in sustainable resource utilization.

Keywords: manganese ore; sintering; phase transitions; hausmannite; braunite; quartz

Academic Editor: Bo Li

Received: 15 December 2024
Revised: 12 January 2025
Accepted: 16 January 2025
Published: 18 January 2025

Citation: Safarov, R.Z.; Baikenov, Y.A.; Zhandildenova, A.K.; Kopishev, E.E.; Kamatov, R.M.; Kargin, J.B.; Sanchez Cornejo, H.; Barnes, C.H.W.; De Los Santos Valladares, L. Phase Transitions and Structural Evolution of Manganese Ores During High-Temperature Treatment. *Metals* **2025**, *15*, 89. https://doi.org/10.3390/met15010089

1. Introduction

Manganese ores are widely used in ferrous metallurgy [1–4]. Manganese, the 12th most abundant element on Earth, constitutes approximately 0.1% of the Earth's crust. Despite this abundance, manganese minerals are often widely dispersed, making it challenging to locate high-grade deposits [5]. The scarcity of high-grade manganese ores results from their consistently high demand [6]. Consequently, attention has shifted toward developing cost-effective technologies for processing medium- and low-grade manganese ores [7,8].

The Central Kazakhstan region hosts numerous medium-grade manganese deposits, with average manganese (Mn) content ranging from 15% to 40%. These deposits are primarily composed of carbonate and oxide ores, which remain underutilized despite their economic potential. Two notable deposits in this region are the Bogach and Zhaksy deposits.

The Bogach manganese ore deposit is located in Central Kazakhstan's Nura district of the Karaganda region. Oxidized ores have earthy and powdery–lumpy textures. Minerals of primary manganese ores are basic braunite ($Mn^{2+}(Mn^{3+})_6SiO_{12}$), hematite ($\alpha$-$Fe_2O_3$), ankerite (less often, $Ca(Fe,Mg,Mn)(CO_3)_2$), friedelite ($Mn^{2+}{}_8Si_6O_{15}(OH,Cl)_{10}$), jacobsite ($(Mn^{2+},Fe^{2+},Mg)(Fe^{3+},Mn^{3+})_2O_4$), and nonmetallic minerals such as calcite ($CaCO_3$), quartz (SiO_2), chlorite, and gypsum ($CaSO_4 \cdot 2H_2O$). Minerals of oxidized manganese ores are pyrolusite ($Mn^{4+}O_2$), psilomelane ($(Ba,H_2O)_2Mn_5O_{10}$), vernadite ($(Mn^{4+},Fe^{3+},Ca,Na)(O,OH)_2 \cdot nH_2O$), hematite, and, less often, hollandite ($(Mn^{4+},Mn^{3+},Ti,Fe^{3+})_8O_{16}$), goethite ($\alpha$-(Mn,Fe)OOH), braunite ($Mn^{2+}(Mn^{3+})_6SiO_{12}$), and jacobsite ($(Mn^{2+},Fe^{2+},Mg)(Fe^{3+},Mn^{3+})_2O_4$. Non-metallic phases include quartz, kaolinite, mica, calcite, and feldspar [9].

The deposit of manganese Zhaksy ore is located in the Zhaksy district of the Akmola region. In the Zhaksy deposit, two genetic types of ores have been recognized: primary, consisting of hollandite and braunite; and secondary (oxidized), consisting of pyrolusite and cryptomelane [10]. The manganese content in primary ores ranges from 7.8% to 53.65%, with an average of 24.7%; the iron content is 6.21%, and the phosphorus content is 0.05%. In ores from the oxidation zone, the manganese content is approximately 30%, the iron content is 4%, and the phosphorus content is 0.06% [11]. According to another origin [10], the amounts of manganese vary from 10% to 16% in the lean ores and up to 50–56% in the massive ores.

Manganese carbonate and oxide ores serve as the primary sources for manganese extraction [12]. Manganese plays a vital role in steel production, contributing to deoxidation and desulfurization processes, as well as functioning as an alloying additive for manufacturing specialized steel grades [13–15].

Most manganese oxide mineral phases are extensively used in industry. Ground natural and synthetic pyrolusite ($MnO_2 \cdot xH_2O$, 63.2% Mn) is utilized in the production of galvanic cells [16], batteries [17,18], and catalysts [19–21]. Braunite ($3\,Mn_2O_3 \cdot MnSiO_3$, 69.5% Mn) is employed in the metallurgical and chemical industries for manganese production [22].

Hausmannite is particularly noteworthy due to its versatile applications, making it a sought-after product in the market [23]. It is used to produce trimanganese tetraoxide, which is applied in manufacturing light brown, yellow–brown, brown, and dark brown bricks, ceramic products, paving slabs, and similar materials. Synthetic hausmannite, as a pigment, is effective for mass or surface staining [23,24], offering higher efficiency compared to pyrolusite. It also reduces harmfulness and labor intensity during production [23]. In addition, the use of hausmannite enhances the quality of painted bricks by reducing water absorption compared to red bricks. It improves the surface structure, making it smoother and more uniform, while also eliminating defects like burnt bubbles.

In recent years, catalytic oxidation has emerged as a promising method for converting toxic volatile organic compounds (VOCs) into less harmful substances, such as CO_2 and

H_2O. Manganese oxides, known for their strong redox properties and significantly lower cost compared to platinum-group metal catalysts, have gained considerable attention [25].

For instance, researchers studied the catalytic activity, hydrothermal stability, and durability of various Mn-based porous oxides ($SmMn_2O_5$, $SmMnO_3$, Mn_3O_4, and Mn_2O_3) in the complete oxidation of ethanol and toluene [26]. Their findings revealed that catalytic performance is highly dependent on the morphology of the materials. Among these, Mn_3O_4, synthesized via a reduction method, demonstrated the highest activity in the oxidation of carbon monoxide and toluene [27].

In manganese ores, manganese occurs as various complex oxides, hydroxides, carbonates, silicates, and, less commonly, sulfides [28]. The most common manganese minerals include the following:

- Oxides and hydroxides: pyrolusite ($MnO_2 \cdot xH_2O$), braunite ($3Mn_2O_3 \cdot MnSiO_3$), hausmannite (Mn_3O_4), manganite ($MnO(OH)$), vernadite ($MnO_2(Mn,Fe,Ca)(O,OH)_2 \cdot nH_2O$), psilomelane ($mMnO \cdot MnO_2 \cdot nH_2O$), hollandite ($MnBaMn_6O_{14}$), and bixbyite ($(Mn,Fe)_2O_3$).
- Carbonates: rhodochrosite ($MnCO_3$), manganocalcite ($(Ca,Mn)CO_3$), kutnahorite, and others.
- Silicates: rhodonite ($(Mn^{2+},Fe^{2+},Mg,Ca)SiO_3$), manganese-containing garnets, olivines ($(Mn,Fe)_2[SiO_4]$), and pyroxenes ($MnMgSi_2O_6$), among others [29].

The oxide content in manganese ores varies due to different geological processes across regions. Phase transitions of oxide components are distinct for each ore type and significantly influenced by high-temperature sintering, which alters the mineralogical composition [30]. This process allows the formation of new oxide components under specific sintering conditions, which depend on the regional characteristics of the deposits.

The scientific challenge addressed in this research is developing methods to obtain target mineral phases, such as braunite (Mn_7SiO_{12}) and hausmannite (Mn_3O_4), from phases where Mn exists in a more oxidized state. Numerous studies [31–34] describe the synthesis of manganese oxide phases, including hausmannite, through methods like co-precipitation, sol-gel synthesis, and hydrothermal synthesis. For example, researchers demonstrated the synthesis of hausmannite in various nanostructures, including plate-like nano-grains, coin-like nano-spheres, and nanopetals, using three distinct protocols: co-precipitation, sol-gel synthesis, and co-precipitation-assisted hydrothermal synthesis [35]. These preparation methods significantly influence the structural, morphological, optical, electrochemical, and magnetic properties of the resulting nanostructured materials.

Studies have also explored high-temperature reduction techniques for manganese ores and their gas reduction behavior. In [36], the high-energy milling method was used to synthesize hausmannite nanoparticles from manganese ores of the West Sumatera deposit (Indonesia). The synthesis involved sintering at over 700 °C and an 8-hour milling duration, producing nanoparticles with a size of 90.50 nm. X-ray fluorescence (XRF) analysis revealed a manganese content of 84.139%, and the hausmannite phase exhibited a tetragonal crystal structure. Furthermore, researchers have shown that high-temperature treatments significantly increase the Mn/Fe ratio in ore samples. At 700 °C over 90 min, the manganese concentration reached 51.89%, with 14.79% iron, resulting in a Mn/Fe ratio of 3.5—approaching ferromanganese-grade specifications [37].

The literature provides examples of thermal transitions between manganese oxide phases, such as MnO, Mn_3O_4, Mn_5O_8, and Mn_2O_3, as a function of temperature [34]. These phase transitions involve structural changes and shifts in the Mn/O ratio across various oxidation states, significantly influencing the material's properties and preparation methods.

Regarding manganese ore reduction, an intriguing study examined the sintering of medium-grade pyrolusite manganese ore from the Karangnunggal mine (West Java, Indonesia) at 1200 °C in methane gas [38]. The findings revealed that pyrolusite (MnO_2)

underwent a reduction process, forming hausmannite (Mn_3O_4), manganosite (MnO), and manganese carbide (Mn_7C_3).

The transformation of MnO_2 to a MnO-rich phase at 950 °C is discussed in [39], which also highlights that increasing the process temperature decreases the oxygen-to-manganese ratio. During these reactions, the oxygen within the oxide structure acts as a reducing agent, oxidizing from O^{-2} to O^0 form when detaching from manganese. The reduction process of MnO_2 to MnO follows this sequence:

$$MnO_2 \rightarrow Mn_2O_3 \rightarrow Mn_3O_4 \rightarrow MnO \quad (1)$$

Sorensen et al. studied manganese ores from Wessels (South Africa), Groote Eylandt (Australia), Companhia Vale do Rio Doce (CVRD, Brazil), and Gabon, which exhibit diverse chemical compositions and complex mineralogical structures [40]. Their findings revealed that MnO_2 is reduced to Mn_2O_3 and Mn_3O_4 during sintering in air. Additionally, when sintered in hydrogen, higher manganese oxides were reduced to MnO, while iron oxides were reduced to metallic iron.

Another study investigated raw manganese ore ($CaMn_6SiO_{12}$) and its sintered forms (Mn_3O_4 and MnO) [41]. Under vacuum conditions, both raw and sintered manganese ore were reduced to MnO at temperatures above 1200 °C. However, in air, manganese ore reduced to Mn_3O_4 instead of MnO at temperatures above 800 °C. The study also determined a higher melting temperature for sintered manganese ore, attributed to its increased MnO content from high-temperature treatment.

Additionally, researchers examined manganese ore from the Clarion–Clipperton Fracture Zone (Cook Islands, Peru Basin) and observed phase transitions after calcination. The main Mn-containing phases, such as asbolane ($NiMn_2O_3(OH)_4 \cdot H_2O$), lithiophorite ($Al_{0.65}H_2Li_{0.33}MnO_4$), manganese oxide ($MnO_2$), vernadite ($Mn(OH)_4$), chalcophanite ($H_6Mn_3O_{10}Zn$), and birnessite ($MnO_2$), transformed into magnetite ($(Mn,Fe)_3O_4$), bixbyite (Mn_2O_3), and manganese oxide (ζMn_2O_3). Calcination reduced the number of phases, resulting in the formation of more thermally stable phases.

Below 1580 °C, all manganese oxides remain in the solid phase, allowing solid-state transformations in reducing atmospheres [42]. The presence of elements like Si can significantly lower the melting point of manganese minerals [43]. The Mn–Mn_xO_y phase stability diagram in Figure 1 [42] illustrates that phase stability depends on temperature and oxygen partial pressure. Increasing temperature at constant oxygen partial pressure destabilizes higher manganese oxides (MnO_2, Mn_2O_3, and Mn_3O_4), reducing them to lower oxidation states. Figure 1 also shows that Mn_3O_4 transitions occur around 1200 °C, and heating MnO at oxygen pressures above 10^{-10} atm leads to melting without a reduction to metallic Mn. This indicates that the thermal decomposition of MnO to metallic Mn is thermodynamically impossible under these conditions. Experimental studies confirm manganese oxides' decomposition to Mn_3O_4 between 900 and 1100 °C [44–46].

The sintering of manganese ores under various conditions facilitates the formation of a wide range of manganese oxide phases. A review of the scientific literature, however, identifies a notable research gap concerning the production of these oxide phases through thermomechanical processing methods. This gap is particularly evident for the manganese ores of Central Kazakhstan, but it also exists at a global level, as few studies detail the specific thermomechanical processes involved in obtaining high-value oxide products from such ores. This underscores the critical importance and timeliness of further research in manganese ore processing to develop technologies for producing valuable oxide phases with industrial applications.

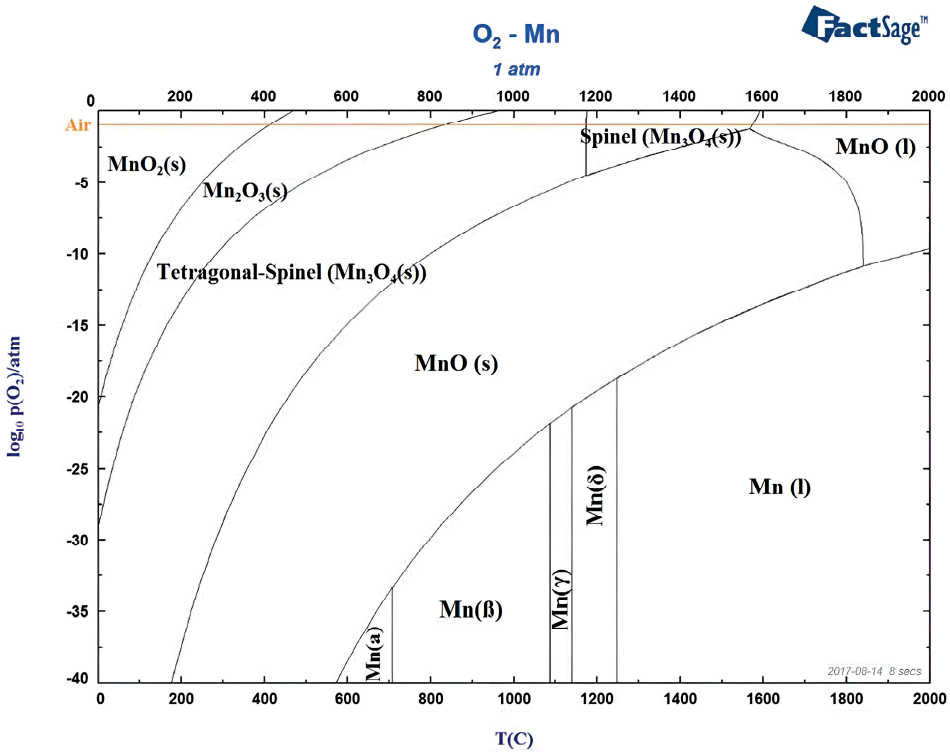

Figure 1. Phase stability diagram of manganese and its oxides. Reprinted with permission from Ref. [42]. Copyright 2025 Taylor & Francis.

In particular, the chemical and mineralogical transformations occurring during the thermal treatment of Central Kazakhstan's manganese ores remain underexplored. The limited understanding of phase evolution and structural changes in these ores significantly impedes their strategic usage for industrial and economic purposes.

Thus, sintering is a high-temperature treatment process that enables the transformation of raw materials into more stable or functional phases by inducing thermal and structural changes. Sintering promotes the decomposition of less stable phases and the emergence of thermally stable manganese oxides. The process induces recrystallization, grain growth, and a reduction in porosity, improving the material's physical and chemical properties. By optimizing sintering conditions, it is possible to establish cost-effective processes to produce high-value materials, addressing challenges tied to the limited availability of high-grade manganese ores.

Advancements in high-temperature sintering technologies have demonstrated considerable potential in converting low- and medium-grade manganese ores into high-value oxide phases such as hausmannite (Mn_3O_4) and braunite ($Mn_7O_{12}Si$). These phases are notable for their applications in catalysis, pigments, and construction materials. Despite this promise, the exact mechanisms and outcomes of sintering processes—particularly for the complex mineralogy of Central Kazakhstan's ores—are still inadequately explored. This gap in knowledge limits the development of cost-effective and efficient processing technologies tailored to the unique characteristics of these regional ores.

The present study seeks to address this gap by investigating the phase transformations, elemental redistribution, and structural evolution within complex metamorphic ores from the Bogach and Zhaksy deposits of Central Kazakhstan subjected to sintering in the temperature range of 600–1200 °C in an air atmosphere. Utilizing advanced analytical techniques such as energy-dispersive X-ray spectroscopy (EDS), X-ray diffraction (XRD), and X-ray fluorescence spectroscopy (XRF), the study examines the correlation between sintering conditions and the elemental and phase compositions of the ores. Additionally,

scanning electron microscopy (SEM) and optical digital microscopy are applied to detail the morphological changes and crystallization patterns in the ore samples.

As part of a broader research initiative, this study contributes to unlocking the potential of Central Kazakhstan's manganese ores by producing technologically valuable oxide phases that can serve as colorants, catalysts, and other industrial materials. The project aims to provide a scientific and technical foundation for developing industries within Kazakhstan that utilize local raw materials. The social and economic implications are significant, offering the potential for competitive industrial growth, regional economic development, and innovation driven by sustainable resource utilization.

2. Materials and Methods

2.1. Sample Preparation

Two manganese ore samples were collected from the Bogach and the Zhaksy deposits (Central Kazakhstan). Table 1 shows reserves and conventional content of Mn in ores of Bogach and Zhaksy deposits according to [11].

Table 1. Reserves of manganese ores of Bogach and Zhaksy deposits.

Deposit	Geographic Coordinates	Reserves, Thousand Tons	Mn Content, %
Bogach (sample 1)	49°44′43.4″ N 68°57′16.5″ E	5000	39.0
Zhaksy (sample 2)	51°56′26.7″ N 67°21′52.1″ E	2300	14.4

The samples were initially in the form of broken rock fragments (lump form). They were crushed using a jaw crusher (Qingdao Decent Group, Qingdao, China) to produce granules ranging from 1 to 5 mm, followed by ball milling for eight hours. Figure 2 presents images of the milled samples, where the ore sample from the Bogach deposit displays a darker shade, nearly black. This darker coloration suggests a higher manganese concentration.

(**a**) (**b**)

Figure 2. Manganese ore samples: (**a**) the Bogach deposit; (**b**) the Zhaksy deposit.

The ground samples were sifted through a sieve with a mesh size of 0.075 mm and subsequently sintered in a muffle furnace (Nanyang Xinyu New Material Technology Co. Ltd, NanYang, China) at temperatures up to 1200 °C. The heating rate was set to 7 °C per minute, and the sintering duration was 4 h. The samples were placed in corundum crucibles for the sintering process.

2.2. X-Ray Powder Diffraction

The samples for X-ray diffraction were manually ground using a mortar and pestle. The samples were mounted in a 25 mm-diameter round holder. The X-ray powder diffraction analysis was performed at room temperature using a D6 Phaser X-ray diffractometer

(Bruker AXS GmbH, Karlsruhe, Germany) with the following configuration: an X-ray source was CuKα 1,2 (λ = 1.5406 Å), with an X-ray generator operated at a voltage of 30–40 kV and a current of 10–15 mA; the goniometer radius was 166.5 mm; and the incident beam optics included a 0.6 mm divergence slit, a 1 mm air-scattering screen, a 0.5 mm Ni air scatter slit, a 2.5° Söller slit, and a 3.0° PSD opening.

The spinning sample stage was used with 10 revolution per minute during the scanning process. The detector was a SSD160-2 Bruker AXS (Bruker AXS GmbH, Karlsruhe, Germany) used in 1D continuous PSD (position-sensitive detector) scan mode. The scan was performed using Bragg–Brentano geometry, between 15 and 85° 2θ. A timestep of 0.8 s, a goniometer step size of 0.02° 2θ, and a number of steps of 3400 were used, resulting in a total measurement time of 47.28 min.

The qualitative analysis was performed using Diffrac.Eva software (version 7.0.0.6); structural data were analyzed after phase identification and were obtained from the Crysrtallography Open Database (COD [47], revision 240108).

The quantitative analysis of crystalline phases and share of amorphous component was performed by means of Rietveld refinement along with internal standard method using Profex software (version 5.4.0) [48]. The average weighted R profile (Rwp) was 2.873 with a standard deviation of 0.77 for Bogach ore samples, and 3.76 with a standard deviation of 0.25 for Zhaksy ore samples. A fully crystalline corundum phase (α-Al_2O_3) was used as a standard. The proportion of the internal standard was 15% of the total mass. The percentages of the amorphous phase and every crystalline phase were calculated using the following equations:

$$K = R_s \frac{100 - W_s}{W_s} \quad (2)$$

$$W_i = \frac{R_i}{K} \quad (3)$$

$$W_{amorph} = 100 - \sum W_i \quad (4)$$

where K is the coefficient of internal standard, R_s and R_i are amounts of internal standard and crystalline phase as determined via the Rietveld method, W_s is the weight percentage of the internal standard (15 wt%), W_i is the weight percentage of the certain crystalline phase, and W_{amorph} is the weight percentage of the amorphous phase.

2.3. X-Ray Fluorescent Spectroscopy

The elemental analysis was performed via X-ray fluorescent spectroscopy (XRF) before and after sintering in each temperature range on an X-ray fluorescence spectrometer S2 Puma (Bruker AXS GmbH, Karlsruhe, Germany). The operating conditions of the device were as follows: tube—Ag; voltage—20–50 kV; current—100–1000 μA; sample rotation—on; automatic filtration; time—~400 s; and atmosphere—vacuum, detector—HighSense XP Silicon Drift Detector (SDD), and limits of detection of elements from Na to Am—1 × 10^{-3}%, excluding Pt and Ag.

For the XRF analysis, we employed the "sandwich" technique to prepare and analyze the ore samples. First, the sample was dried after being crushed and sieved through a 0.071 mm mesh. Once dried, approximately 5 grams of the sample was weighed using an analytical balance. A boric acid substrate weighing 9 grams was prepared to act as a support layer, ensuring that the pressed pellet achieved a thickness of 6–7 mm, which is optimal for analysis. The boric acid was placed in the die to form the bottom layer of the "sandwich" and manually pressed at 5 tons to create a stable foundation. The ore sample was then evenly distributed on top of the boric acid layer and pressed further at 25 tons for 3–5 min to form a cohesive pellet. To prevent cracking during vacuum measurement, the pressure was released gradually in intervals of 20–30 s, reducing by 5 tons at each step. The

resulting pressed pellet, with boric acid as the support and the ore sample as the top layer, was placed in a measurement ring for XRF analysis. This method ensures that the sample is properly supported and prepared for accurate XRF measurements by creating a stable and uniform pellet that can withstand vacuum conditions during analysis.

2.4. Scanning Electron Microscopy

Surface characterization techniques were employed to analyze the morphology and composition of the manganese ores samples before and after sintering using a scanning electron microscope Axia ChemiSEM (SEM) (Thermo Fisher Scientific, Waltham, MA, USA) with Everhart-Thornley detector (ETD, secondary electrons) and concentric backscatter detector (CBS, backscattered electrons) at an accelerating voltage of 20 kV. Elemental analysis and mapping were performed using an equipped energy-dispersive X-ray spectroscopy detector (EDS). Particle size distribution on micrographs was studied using the software Image-Pro V11.0.4 (Media Cybernetics, Washington, DC, USA).

2.5. Optical Microscopy

A Leica DVM 5000 HD (Leica Microsystems, Heerbrugg, Switzerland) digital microscope was used to obtain micrographs of the studied materials in their initial state and after the sintering process. Micrographs were captured at magnifications of ×100 and ×200 using artificial reflected light illumination. Pixel intensity distributions on optical micrographs were analyzed using software ImageJ V1.54 (National Institutes of Health, Bethesda, MD, USA) [49].

3. Results and Discussion

3.1. Elemental Content of Products

The elemental compositions of the initial ore samples and samples sintered at different temperatures were obtained using XRF. Table 2 presents defined elemental compositions of the samples.

Table 2. Results of studying the effect of sintering temperature on the elemental composition of studied samples using XRF analysis (sintering duration: 4 h).

T, °C	Elemental Content, wt.%												
	Bogach												
	Mn	Ca	Si	Ba	K	Sr	Fe	Mg	Al	Pb	Zn	Na	Ti
25	60.77	5.44	3.49	2.05	2.04	1.42	0.89	1.00	0.82	0.21	0.09	0.04	0.05
300	60.74	5.86	3.42	2.04	2.04	1.43	0.88	1.00	0.81	0.21	0.09	0.03	0.05
400	62.8	6.1	3.58	2.11	2.12	1.47	0.91	1.03	0.82	0.22	0.09	0.02	0.05
500	62.7	6.04	3.57	2.11	2.11	1.46	0.9	1.06	0.8	0.22	0.09	0.05	0.05
600	63.48	6.08	3.78	2.14	2.13	1.48	0.94	1.06	0.88	0.23	0.1	0.04	0.05
800	64.32	6.32	4.26	2.18	2.12	1.49	1.01	1.15	1.15	0.23	0.1	0.03	0.05
900	65.57	6.18	3.73	2.14	2.02	1.54	0.96	1.04	0.91	0.24	0.1	0.12	0.05
1000	65.37	5.65	3.74	2.12	1.39	1.59	1.00	0.86	0.96	0.2	0.1	0.09	0.04
1100	65.7	4.63	2.6	1.86	1.55	1.56	0.95	0.82	0.68	0.22	0.1	0.19	0.03
1200	65.24	4.45	2.75	1.82	1.59	1.51	0.95	0.76	0.58	0.18	0.11	0.02	0.03

Table 2. *Cont.*

T, °C	Elemental Content, wt.%												
	Zhaksy												
	Mn	Ca	Si	Ba	K	Sr	Fe	Mg	Al	Pb	Zn	Na	Ti
25	44.88	0.76	20.85	0.38	1.38	0.21	6.14	0.30	2.66	0.02	0.03	0.04	0.10
300	42.99	0.73	19.95	0.37	1.32	0.20	5.89	0.31	2.58	0.02	0.03	0.06	0.10
400	44.55	0.75	21.12	0.38	1.37	0.20	6.12	0.32	2.73	0.02	0.03	0.06	0.10
500	44.35	0.75	20.61	0.38	1.36	0.20	6.09	0.31	2.65	0.02	0.03	0.08	0.10
600	44.10	0.74	19.71	0.37	1.33	0.21	6.10	0.30	2.60	0.02	0.03	0.09	0.10
800	45.14	0.76	21.28	0.41	1.42	0.20	6.21	0.37	2.79	0.02	0.03	0.28	0.10
900	45.68	0.75	19.83	0.41	1.32	0.21	6.23	0.38	2.64	0.02	0.03	0.35	0.10
1000	45.52	0.74	17.15	0.44	1.21	0.22	6.00	0.34	2.36	0.03	0.03	0.18	0.10
1100	43.74	0.68	12.90	0.45	1.11	0.22	5.69	0.29	1.89	0.03	0.03	0.13	0.09

For the Bogach ore sample in the initial state (25 °C), manganese is the dominant element at 60.77 wt.%, followed by calcium (5.44 wt.%) and silicon (3.49 wt.%). Other elements present in smaller quantities include barium, potassium, strontium, iron, magnesium, aluminum, lead, zinc, sodium, and titanium. As the sintering temperature increases, several trends become apparent. The manganese content gradually increases from 60.77 wt.% at room temperature to a maximum of 65.7 wt.% at 1100 °C, showing slight fluctuations at higher temperatures. The increase in manganese content corresponds to its transition from more oxidized to more reduced states. For example, the theoretical manganese content in pyrolusite (MnO_2) is 63.2 wt.%, which increases to 72 wt.% in more reduced phases, such as hausmannite (Mn_3O_4), and reaches 77.4 wt.% in manganosite (MnO).

Calcium content initially increases slightly up to 800 °C (reaching 6.32 wt.%) but then decreases significantly at higher temperatures, dropping to 4.45 wt.% at 1200 °C. Silicon content shows some variation, peaking at 800 °C (4.26 wt.%) before decreasing to 2.75 wt.% at 1200 °C. Minor elements also show temperature-dependent changes. Elements like barium, potassium, and aluminum generally maintain stable concentrations up to 800 °C but show decreased content at higher temperatures. Strontium shows a slight increase with a temperature up to 1100 °C. The concentrations of iron, magnesium, lead, zinc, sodium, and titanium remain relatively stable throughout the temperature range, with only minor fluctuations.

During sintering at elevated temperatures (from 25 °C to 1100 °C), the Mn content increases. This occurs primarily due to the decomposition of other compounds and the relative concentration of elements. As the temperature rises, volatile components and some less stable compounds may decompose or evaporate, leading to a relative increase in the concentration of more stable elements like manganese. Additionally, the high-temperature treatment can cause the transformation of manganese-containing phases into more stable forms, potentially concentrating the manganese content in the remaining material.

The XRF analysis data for Zhaksy ore shows different compositional characteristics and temperature-dependent behavior compared to Bogach ore. In the initial state (25 °C), the manganese content is notably lower at 44.88 wt.%, while the silicon content is significantly higher at 20.85 wt.%. Iron is present in higher quantities (6.14 wt.%), and aluminum shows a higher content (2.66 wt.%) compared to Bogach ore. Calcium content is much lower at 0.76 wt.%. As the sintering temperature increases, the changes in elemental composition show different trends. The manganese content shows slight fluctuations, reaching a maximum of 45.68 wt.% at 900 °C and then decreasing to 43.74 wt.% at 1100 °C. Additionally, for the ore from the Zhaksy deposit, no clear trends in manganese content variation are

observed. This indicates that notable changes in the qualitative phase composition do not occur.

Silicon content remains relatively stable up to 800 °C (around 20–21 wt.%) but shows a significant decrease at higher temperatures, dropping to 12.90 wt.% at 1100 °C. Iron content remains relatively stable throughout the temperature range (5.69–6.23 wt.%). The aluminum content follows a similar pattern to silicon, maintaining stability up to 800 °C (around 2.6–2.8 wt.%) before decreasing to 1.89 wt.% at 1100 °C. Other elements like barium, potassium, strontium, magnesium, lead, zinc, sodium, and titanium show minor variations but generally maintain low concentrations throughout the temperature range. This composition and behavior suggest different mineralogical phases and transformations compared to the Bogach ore, with a notably higher silicon and iron content indicating a different type of manganese mineralization.

3.2. Phase Content of Products

Figure 3 presents the X-ray diffraction patterns of the samples in their initial state (25 °C) and after sintering at various temperatures ranging from 800 °C to 1200 °C. The characteristic diffraction reflections are marked, enabling the identification of the phases present using the COD (Crystallography Open Database).

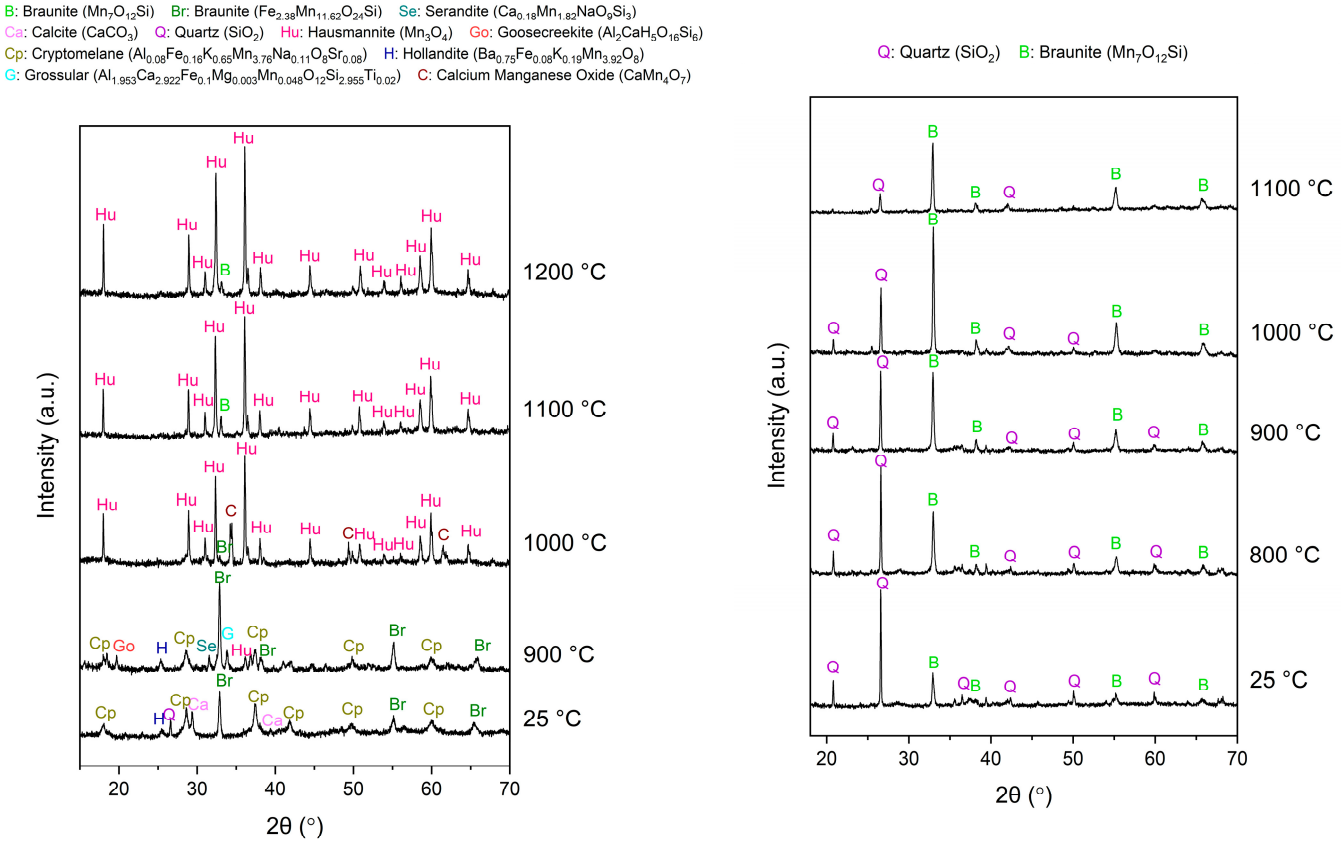

(**a**) (**b**)

Figure 3. X-ray diffractograms of the Bogach (**a**) and Zhaksy (**b**) manganese ore samples after sintering during 4 h.

In the initial state, the ore sample from the Bogach deposit (Figure 3a) contains cryptomelane, braunite, calcite, and quartz as the dominant phases. The most intense diffraction peaks of cryptomelane are observed at 2θ angles of 18.269°, 28.855°, 37.554°, 41.556°, 50.151°, and 60.726°. Braunite is identified with distinct peaks at 32.856°, 54.998°, and

65.602°. Additionally, associated minerals such as calcite (peaks at 29.399° and 39.406°) and quartz (peak at 26.566°) are present.

Moreover, the hollandite phase appears to be present in the sample, characterized by numerous low-intensity peaks, with the strongest peak observed at 2θ = 25.236°.

After the Bogach sample was sintered at 900 °C, the number of detected crystalline phases increased. In addition to the initial phases, new phases were identified, probably including goosecreekite (strongest peak at 2θ = 19.802°), serandite (strongest peak at 2θ = 33.633°), and grossular (strongest peak at 2θ = 33.819°).

Furthermore, at this temperature, a small reflection corresponding to the strongest peak of the hausmannite phase was detected at 2θ = 36.135°. Notably, the peak corresponding to quartz disappeared, while the peaks of braunite became more intense. An additional peak of braunite was also observed at 2θ = 38.138°.

After the Bogach sample was sintered at 1000 °C, the variety of crystalline phases decreased, and a significant phase transition occurred, resulting in the formation of the hausmannite phase. In the diffraction pattern, hausmannite was identified with several distinct peaks at 2θ angles of 18.041°, 28.961°, 31.041°, 32.442°, 36.135°, 38.168°, 44.472°, 50.940°, 53.947°, 56.115°, 58.586°, 60.014°, and 64.711°. These peaks correspond precisely to the reference data for hausmannite in the COD database (COD1514121).

Notably, the braunite phase almost disappeared from the diffraction pattern, with only its strongest peak at 2θ = 32.856° remaining visible as a minor reflection. Additionally, a new structure, possibly calcium manganese oxide ($CaMn_7O_{12}$ and COD2104444), was observed, with its strongest peaks appearing at 2θ angles of 34.196°, 49.498°, and 61.481°.

When the sintering temperature was increased to 1100 °C and 1200 °C, the diffraction patterns of the Bogach sample showed peaks corresponding exclusively to the hausmannite and braunite phases. Notably, the intensity of the hausmannite peaks increased with a rising temperature.

For the braunite phase, a structural change was observed: at 25–1000 °C, the structure corresponded to $Fe_{2.38}Mn_{11.62}O_{24}Si$ (COD9000774), while at 1100–1200 °C, it shifted to $Mn_7O_{12}Si$ (COD9000532). Additionally, the peak intensity of braunite decreased significantly when sintering was performed at 1200 °C.

In the initial state, the ore sample from the Zhaksy deposit (Figure 3b) contained only quartz and braunite phases. The most intense diffraction peaks of quartz were observed at 2θ angles of 20.840°, 26.621°, 36.511°, 42.412°, 50.106°, and 59.903°. The peaks of braunite were less intense, with the strongest peak at 2θ = 32.983°, accompanied by less distinct peaks at 2θ angles of 38.158°, 55.317°, and 65.703°. Additionally, the hematite phase was identified in the diffraction pattern, represented by a series of small peaks that become visible upon closer magnification of the diffractogram.

Notably, after sintering, no additional phases were detected. However, the intensity of the quartz peaks decreased with an increasing temperature. In contrast, the braunite peaks became more pronounced after sintering. The intensity of the strongest braunite peak became approximately equal to that of the strongest quartz peak after sintering at 900 °C. At 1100 °C, braunite became the dominant crystalline phase.

The Rietveld refinement method, incorporating an internal standard, was employed for quantitative phase analysis (QPA). Corundum (Al_2O_3, COD1000032) was used as the internal standard. Figures 4 and 5 present the results of the refinement process. The refinement was performed in automatic mode using the Profex software.

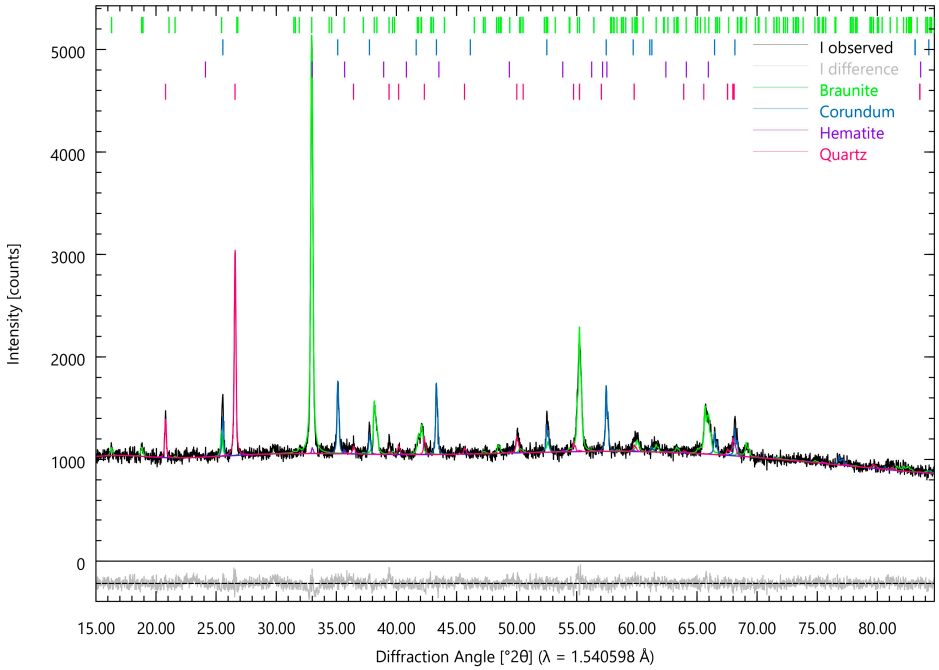

Figure 4. Rietveld refinement for Zhaksy ore sample sintered under 1000 °C with corundum (Al_2O_3, COD1000032) as internal standard (R_{wp} 3.33).

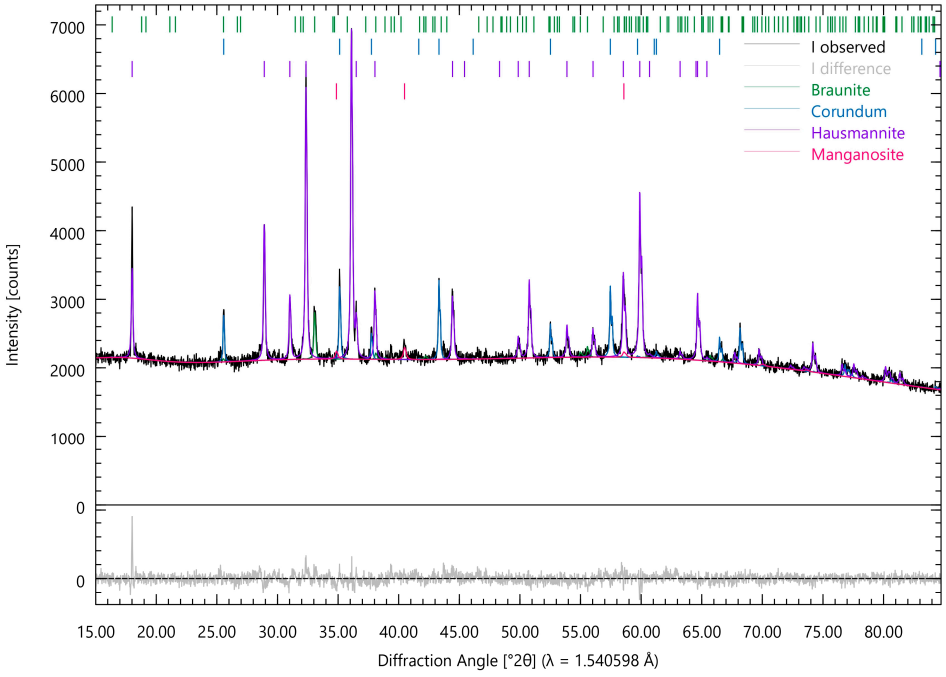

Figure 5. Rietveld refinement for Bogach ore sample sintered under 1100 °C with corundum (Al_2O_3, COD1000032) as internal standard (R_{wp} 2.73).

Following the Rietveld refinement, a good visual agreement between the experimental and calculated diffraction patterns was achieved for all samples. The average R_{wp} values were 2.873 for samples of Bogach ore and 3.765 for samples of Zhaksy ore. Since these R_{wp} values are well below the commonly accepted threshold of 10, the results of the Rietveld refinement were deemed satisfactory.

Figures 6 and 7 illustrate the results of quantitative phase analysis (QPA) for the studied ores. The use of the internal standard method enabled the calculation of the amorphous phase content. In the non-sintered samples, the amorphous phase accounted for 57.6 wt.% in the Bogach ore and 71.0 wt.% in the Zhaksy ore.

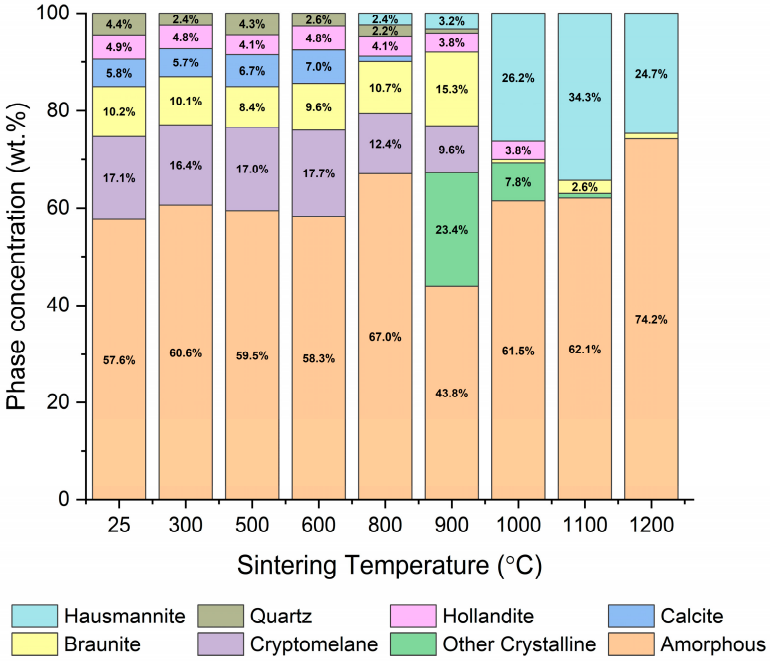

Figure 6. Rietveld refinement-based quantity phase analysis results for Bogach ore samples sintered. Hausmannite—Mn_3O_4, COD1514121; braunite—$Fe_{2.38}Mn_{11.62}O_{24}Si$, COD9000774 for 25–1000 °C, and $Mn_7O_{12}Si$, COD9000532 for 1100–1200 °C; quartz—SiO_2, COD 9005019, cryptomelane—$Al_{0.08}Fe_{0.16}K_{0.65}Mn_{3.76}Na_{0.11}O_8Sr_{0.08}$, COD9007647; hollandite—$Ba_{0.75}Fe_{0.08}K_{0.19}Mn_{3.92}O_8$, COD9009727; calcite—$CaCO_3$, COD9000095; Other Crystaline: hematite—Fe_2O_3, COD 9000139; goosecreekite—$Al_2CaH_5O_{16}Si_6$, COD9001040; serandite—$Ca_{0.18}Mn_{1.82}NaO_9Si_3$, COD9000488; grossular—$Al_{1.953}Ca_{2.922}Fe_{0.1}Mg_{0.003}Mn_{0.048}O_{12}Si_{2.955}Ti_{0.02}$, COD9017181; spinel—$Al_{2.401}Mg_{0.398}O_4$, COD9005768; calcium manganese oxide ($CaMn_7O_{12}$, COD2104444).

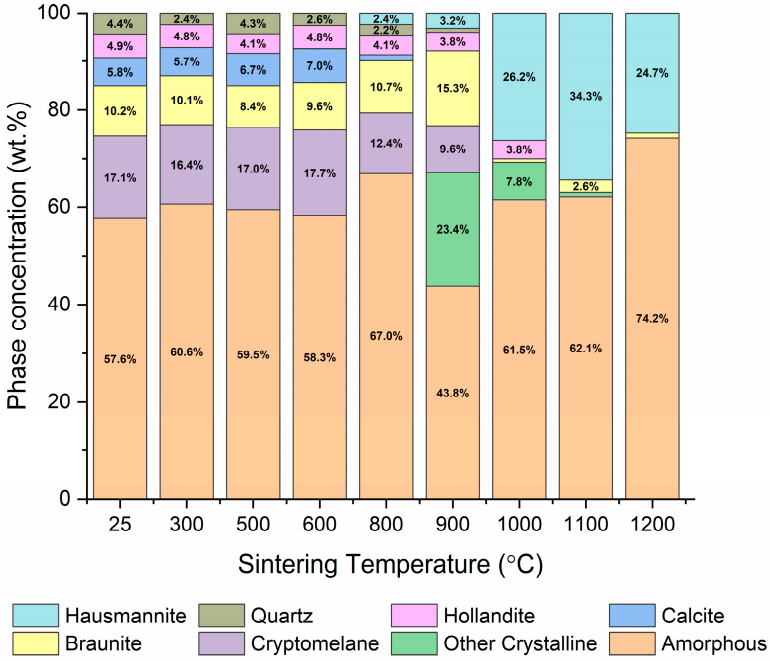

Figure 7. Rietveld refinement-based quantity phase analysis results for Zhaksy ore samples sintered. Hematite—Fe_2O_3, COD9000139; quartz—SiO_2, COD9010145; braunite—$Mn_7O_{12}Si$, COD9006541.

We observed a gradual increase in the amorphous content with an increasing sintering temperature. At a critical point of a significant phase composition change, the amorphous phase content decreased sharply, followed by a subsequent increase with further temperature rise. The temperature at which the phase composition changed significantly was determined to be 900 °C.

Additionally, Tables 3 and 4 provide the results of the semi-quantitative phase content analysis, including the degree of crystallinity (DOC) values calculated using the internal standard method.

Table 3. Semi-quantitative analysis of crystalline phase ratios in Bogach ore samples, based on Rietveld refinement, in their initial state and after sintering for 4 h.

Phase	25 °C	300 °C	400 °C	500 °C	600 °C	800 °C	900 °C	1000 °C	1100 °C	1200 °C
Cryptomelane $Al_{0.08}Fe_{0.16}K_{0.65}Mn_{3.76}Na_{0.11}O_8Sr_{0.08}$, COD9007647	40.26	41.62	40.17	42.04	42.33	37.51	17.07	-	-	-
Braunite $Fe_{2.38}Mn_{11.62}O_{24}Si$, COD9000774	24.18	25.56	23.39	20.73	23.12	32.29	27.28	1.82	-	-
Braunite $Mn_7O_{12}Si$, COD9000532	-	-	-	-	-	-	-	-	6.75	4.23
Calcite $CaCO_3$, COD9000095	13.62	14.49	15.25	16.51	16.71	3.76	-	-	-	-
Hollandite $Ba_{0.75}Fe_{0.08}K_{0.19}Mn_{3.92}O_8$, COD9009727	11.59	12.18	11.68	10.02	11.58	12.49	6.85	9.89	-	-
Quartz SiO_2, COD 9005019	10.34	6.14	9.50	10.71	6.26	6.67	1.48	-	-	-
Hausmannite Mn_3O_4, COD1514121	0.00	0.00	0.00	0.00	0.00	7.28	5.65	68.04	90.45	95.77
Manganosite * MnO, COD1514229	-	-	-	-	-	-	-	-	2.80	-
Goosecreekite * $Al_2CaH_5O_{16}Si_6$, COD9001040	-	-	-	-	-	-	7.36	-	-	-
Serandite * $Ca_{0.18}Mn_{1.82}NaO_9Si_3$, COD9000488	-	-	-	-	-	-	8.25	-	-	-
Grossular * $Al_{1.953}Ca_{2.922}Fe_{0.1}Mg_{0.003}Mn_{0.048}O_{12}Si_{2.955}Ti_{0.02}$, COD9017181	-	-	-	-	-	-	8.45	-	-	-
Spinel * $Al_{2.401}Mg_{0.398}O_4$, COD9005768	-	-	-	-	-	-	17.62	-	-	-
Frankdicksonite * BaF_2, COD9009004	-	-	-	-	-	-	-	1.48	-	-
Calcium manganese oxide * $CaMn_7O_{12}$, COD2104444	-	-	-	-	-	-	-	18.77	-	-
DOC, %	42.4	39.4	49.6	40.5	41.7	33.0	56.2	38.5	37.9	25.8
R_{wp}	2.61	2.56	2.56	2.61	2.57	2.5	5.05	2.76	2.73	2.78

* Possible phases found as the most suitable from COD through the consistency of the strongest peaks.

Table 4. Semi-quantitative analysis of crystalline phase ratios in Zhaksy ore samples, based on Rietveld refinement, in their initial state and after sintering for 4 h.

Phase	25 °C	300 °C	400 °C	500 °C	600 °C	800 °C	900 °C	1000 °C	1100 °C
Braunite $Mn_7O_{12}Si$, COD9006541	34.03	33.35	33.09	31.30	32.50	45.71	60.04	74.97	83.81
Quartz SiO_2, COD 9010145	58.08	57.85	58.83	59.71	58.60	44.31	33.95	23.90	16.19
Hematite Fe_2O_3, COD9000139	7.89	8.81	8.08	8.99	8.91	9.98	6.01	1.14	-
DOC, %	29.0	26.0	25.9	27.3	27.5	40.2	39.6	36.99	26.87
R_{wp}	3.84	3.95	3.93	4.00	4.01	3.77	3.63	3.33	3.43

After 900 °C, the hausmannite content in the crystalline component of the Bogach ore samples increased sharply, reaching 90.45 wt.% at 1100 °C. Subsequently, the rate of increase slowed, with hausmannite accounting for 95.77 wt.% of the crystalline component at 1200 °C. Concurrently, the degree of crystallinity decreased significantly, from 56.2% at 900 °C to 25.8% at 1200 °C.

The quartz content gradually declined, starting from 10.34 wt.% in the initial state (25 °C) to 1.48 wt.% at 900 °C. After sintering at higher temperatures, quartz was no longer

detected in the diffraction patterns. At 900 °C and 1000 °C, diffraction peaks corresponding to several unstable crystalline phases were observed, contributing to an increase in the DOC. However, with further temperature increases, these phases likely transformed into the more thermally stable hausmannite phase or transitioned into an amorphous state, resulting in a gradual increase in the amorphous phase content.

When studying the Zhaksy ore samples, a sharp increase in the degree of crystallinity (DOC) was observed at 800 °C. At this temperature, the amounts of crystalline braunite and quartz were nearly equal, while the hematite content remained relatively high at 9.98 wt.%. At higher temperatures, quartz and hematite underwent amorphization, leading to a decrease in DOC. By 1100 °C, the crystalline quartz content had decreased from 58.08 to 16.19 wt.%, and hematite was no longer detectable. Concurrently, the braunite content within the crystalline phase increased to 83.81 wt.%.

Sintering at temperatures above 1100 °C leads to the melting of Zhaksy ore, while Bogach ore begins to melt at temperatures exceeding 1200 °C. The conditions for melt formation depend on the ore composition, with quartz apparently playing a crucial role. Even though pure quartz melts around 1700 °C, its interaction with dispersed fluxes—in a fine-grained, partially amorphous state—lowers the effective melting point by creating eutectic melts at lower temperatures. By contrast, the Bogach ore generally contains fewer fluxing components and a higher proportion of thermally stable manganese oxides, delaying the onset of melting until temperatures exceed 1200 °C.

This phenomenon is akin to surface melting or thermal softening in multi-component systems, where the presence of minor phases and their chemical interactions ultimately determine how early a melt phase appears.

Operations involving the melt are challenging because of the high hardness of manganese ore melts. This hardness complicates sample preparation for analyses such as X-ray powder diffraction (XRD) and X-ray fluorescence (XRF) using the pressed pellet method. Additionally, the high hardness of the melts makes it difficult to prepare powdered products for further characterization. Finally, it is important to note that melting processes fall outside the scope of this study, which focuses exclusively on the sintering process.

Table 5 presents the structural parameters of the hausmannite (Mn_3O_4) and braunite ($Mn_7O_{12}Si$) crystalline phases obtained after ore sintering, analyzed using Rietveld refinement in Profex software. For the hausmannite phase, derived from Bogach ore sintered at 1200 °C, the lattice parameters indicate a tetragonal crystal system with space group $I4_1/a_2/m_2/d$ and lattice parameters a = b = 5.763 Å and c = 9.439 Å. The phase exhibits a very low lattice strain (9.4×10^{-7}), suggesting minimal lattice distortions. The average crystallite size is relatively small at 113.4 ± 4.5 nm, indicating fine crystallites, which may enhance material reactivity. The density of 4.848 g/cm^3 and an R-phase value of 4.17% indicate a good fit between experimental and calculated diffraction data.

Table 5. Structural and crystallographic parameters of hausmannite and braunite crystalline phases obtained after ore sintering, calculated using Rietveld refinement in Profex software.

Crystalline Phase	Ore	Sintering Temperature, °C	Lattice Strain	Lattice Parameters, Å	Average Crystallite Size (Isometric), nm	Density, g/cm^3	R-phase, %	Crystal System	Spacegroup
Hausmannite Mn_3O_4, COD1514121	Bogach	1200	9.4×10^{-7}	a = b = 5.763 c = 9.439	113.4 ± 4.5	4.848	4.17	tetragonal	$I4_1/a_2/m_2/d$
Braunite $Mn_7O_{12}Si$, COD9006541	Zhaksy	1100	73.6×10^{-7}	a = b = 9.436 c = 18.769	176.0 ± 34.0	4.806	4.01	tetragonal	$I4_1/a_2/c_2/d$

For the braunite phase, derived from Zhaksy ore sintered at 1100 °C, the lattice parameters also correspond to a tetragonal crystal system but with space group $I4_1/a_2/c_2/d$, and lattice parameters a = b = 9.436 Å and c = 18.769 Å. This phase shows a significantly higher lattice strain (73.6×10^{-7}), indicating more pronounced lattice distortions, potentially due to differences in composition. The average crystallite size is larger at 176.0 ± 34.0 nm, suggesting coarser crystallites compared to hausmannite. The density of 4.806 g/cm^3 and an R-phase value of 4.01% also confirm a reliable refinement. Thus, the hausmannite phase exhibits smaller crystallites and a lower lattice strain compared to braunite, which may reflect differences in their formation mechanisms and structural stability under the given sintering conditions.

3.3. Scanning Electron Micrographs of the Studied Samples

Manganese ore samples were analyzed using SEM with an Axia ChemiSEM (Thermo Fisher Scientific, USA). The integrated EDS system facilitated the analysis of elemental distribution alongside capturing micrographs of the samples. Figure 8 displays micrographs of Zhaksy ore samples in their initial state and after sintering at 900 °C and 1100 °C. Elemental mapping was performed by assigning distinct colors to different elements based on EDS results. The primary elements detected were Mn, Si, and O, which align well with the findings of XRF analysis. In Figure 8, Mn is represented in purple, while Si is depicted in yellow. The use of contrasting colors enabled the visual assessment of the spatial distribution of the phases.

According to the XRD results, the dominant crystalline phases in the Zhaksy ore samples were identified as braunite ($Mn_7O_{12}Si$) and quartz (SiO_2). Therefore, it can be inferred that the areas highlighted in purple (Mn) correspond to the braunite phase, whereas the areas highlighted in yellow (Si) predominantly represent quartz. Although Si is also present in braunite, its concentration in this phase is significantly lower.

The comparison of the micrographs enables us to track changes in the surface structure of Zhaksy ore samples at different scales after the sintering process. In the initial state, the samples consist of dense, nonuniform particles of varying sizes, ranging from 50 μm to 1 μm (Figure 8a). The nonuniformity in particle size is likely due to manual sample preparation using a pestle and mortar. Two distinctly highlighted components are visible in the micrographs, likely corresponding to braunite and quartz. However, the particle structures in this state are relatively similar, making it difficult to clearly distinguish between these two phases. XRD analysis indicates that the degree of crystallinity (DOC) for this sample is low, with 71 wt.% of the material being amorphous. This high amorphous content likely prevents the formation of well-defined crystalline structures.

Under higher magnification (×8000), the surface appears dense and lacks significant porosity (Figure 8b). At this scale, the distribution of the two phases becomes more distinct, with clearer delineation between the braunite and quartz regions.

Based on the XRD results, significant changes in the phase composition of crystalline components were first observed at 900 °C. Correspondingly, alterations in the surface structure were evident (Figure 8c). At this temperature, roundish particles with uneven surfaces began to form, likely corresponding to microcrystals generated during thermal processes. Additionally, particles with sharp edges appeared coated with clusters of irregularly shaped microcrystals. The distribution of Mn and Si atoms remained discernible, although the contrast between these elements became less pronounced.

At a magnification of ×8000, the surface exhibited a less uniform appearance. An agglomeration of particles occurred, leading to an increase in their size, while small-sized pores began to form (Figure 8d). Crystals lacked distinct geometric forms and often appeared as flake-like structures, though occasionally straight crystal edges were visible.

Despite these changes, the visual distribution of Mn- and Si-containing phases remained observable, underscoring the transformation dynamics induced via sintering.

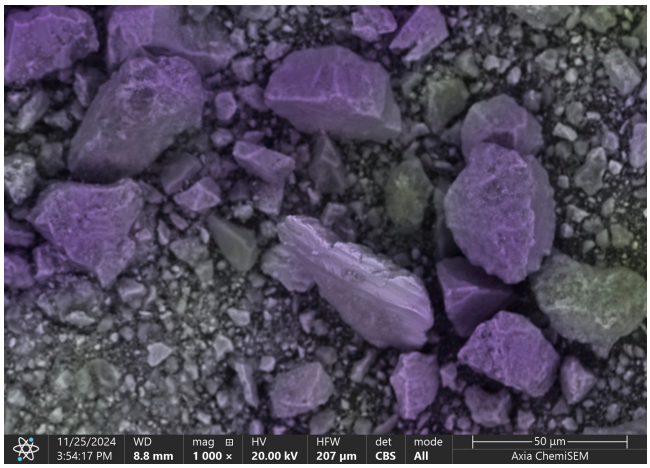

(**a**)

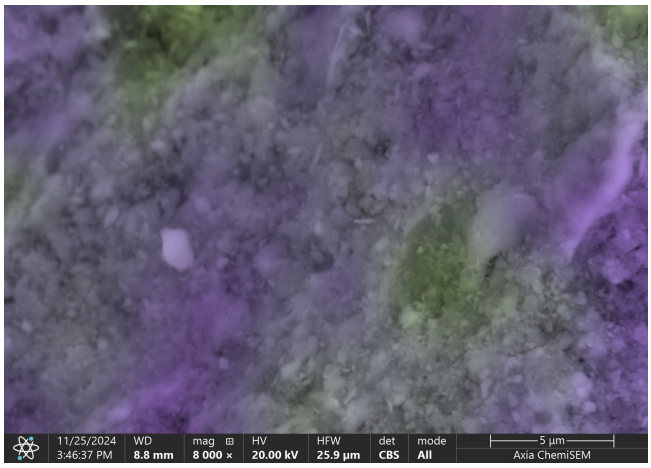

(**b**)

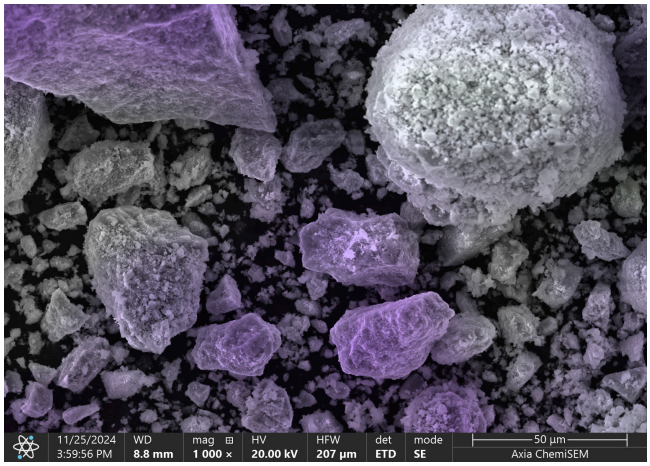

(**c**)

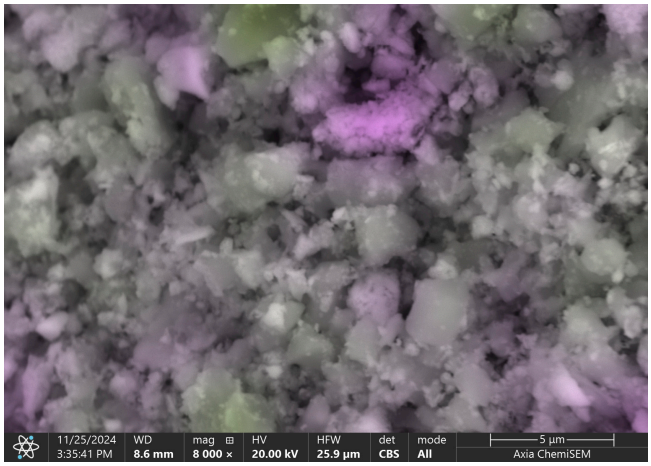

(**d**)

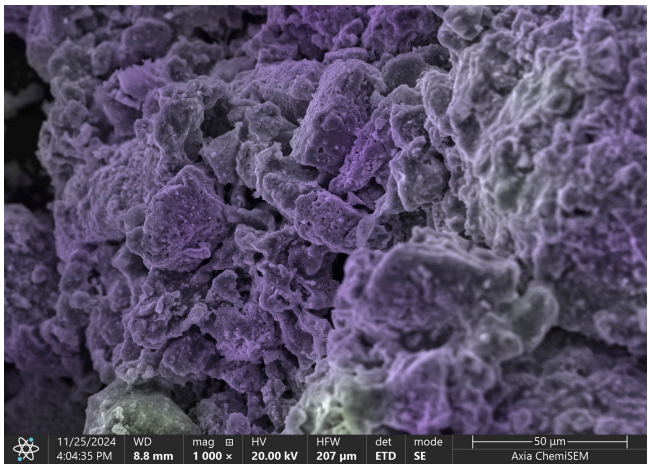

(**e**)

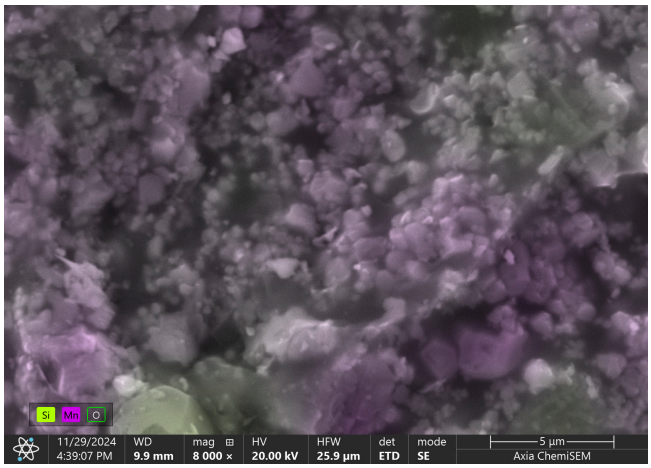

(**f**)

Figure 8. Micrographs of Zhaksy ore samples: (**a**) in initial state (×1000); (**b**) in initial state (×8000); (**c**) after sintering at 900 °C (×1000); (**d**) after sintering at 900 °C (×8000); (**e**) after sintering at 1100 °C (×1000); and (**f**) after sintering at 1100 °C (×8000). Mn atoms highlighted in purple; Si atoms highlighted in yellow.

The micrograph Figure 8e depicts the sintered Zhaksy manganese ore at 1100 °C at a 1000× magnification. The visible structure shows a highly irregular, porous, and granular morphology. The sintering process has caused the particles to partially fuse, forming a network of interconnected grains and voids. These voids or pores are likely due to gas evolution during sintering or incomplete densification. The manganese-rich regions, highlighted in purple, are predominant in the image, indicating a significant concentration of manganese across the structure. This observation aligns with the XRD results, which demonstrate an increase in braunite crystallization as quartz becomes more amorphous during heat treatment. The granular forms appear relatively rough, with surface textures reflecting transformations caused by thermal processes. The presence of yellow-colored Si-containing phase is minimal in this specific field of view, suggesting that manganese is the primary constituent of this area, with silicon potentially localized in separate regions or as part of secondary phases. The observed features are relatively small (micron-scale), with distinct boundaries between grains.

Under higher magnification (×8000), the micrograph of the Zhaksy ore sample sintered at 1100 °C reveals a granular and rough morphology typical of sintered materials. Manganese-rich regions (in purple) dominate the visual field, appearing as interconnected granular phases, with a diffuse presence of silicon-rich areas (yellow–green) interspersed throughout. The transition zones between manganese and silicon phases appear more gradual, potentially indicating partial diffusion or interaction during the sintering process. The surface shows irregular textures with microvoids and slight porosity, likely a result of gas evolution or incomplete fusion. The microstructure suggests a mixture of manganese and silicon phases, with some degree of homogeneity in certain areas and localized phase segregation in others.

Thus, in the initial state, the surface appears relatively smooth and uniform, with smaller, rounded particles and minimal porosity. After sintering at 900 °C, the surface shows noticeable changes. The particles have begun to agglomerate, forming larger clusters with increased porosity. The texture becomes rougher as partial fusion occurs, and manganese-rich areas become more pronounced. With sintering at 1100 °C, the transformation is more pronounced. The particles have further fused into larger, interconnected structures with visible porosity. The texture is even rougher and more complex, reflecting significant recrystallization and phase development. The high temperature enhances particle bonding and manganese concentration, altering the material's properties.

Different locations on the micrographs of Zhaksy ore samples, both in their initial state and after sintering at 1100 °C, were analyzed using point EDS elemental analysis. Figure 9 illustrates the specific locations where spectra were collected, and the corresponding results of the elemental analysis are summarized in Table 6.

The analysis was focused on the primary elements present in the samples—Mn, Si, and O. Initially, the ore shows varying manganese and silicon content, indicating the presence of phases like braunite and quartz. Points 2, 3, and 7, with higher manganese, likely correspond to braunite-rich regions. Points 4 and 5, with elevated silicon, represent quartz-rich areas. The high oxygen content suggests the presence of oxides, consistent with a significant amorphous phase in the initial samples. After sintering at 1100 °C, manganese distribution becomes more uniform with slight fluctuations in silicon content, reflecting thermal effects on the phases. Increased manganese at points 2, 6, 7, and 8 indicates enhanced braunite crystallization. Point 9, with higher silicon, may still represent quartz, though its distinctiveness decreases, aligning with quartz amorphization observed during sintering. These changes align with phase transformations due to heat treatment, leading to morphological changes such as microcrystalline structures, confirming braunite and quartz as dominant phases with significant reorganization during sintering.

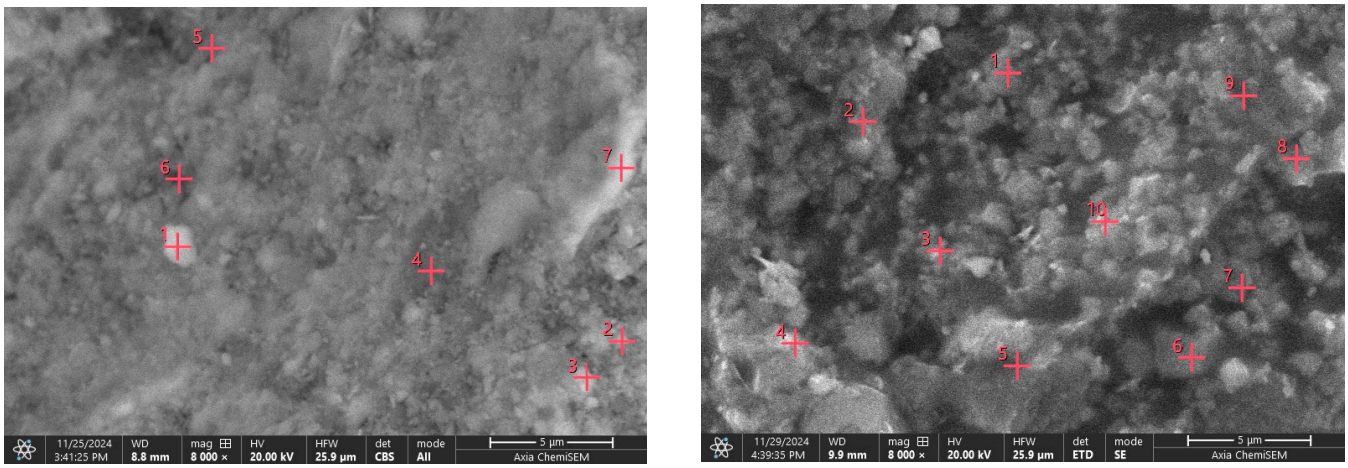

(**a**) (**b**)

Figure 9. Micrographs of Zhaksy ore sample in initial state (**a**) and after sintering at 1100 °C (**b**) with points for EDS.

Table 6. Mn, Si, and O content in samples of Zhaksy ore analyzed via EDS using AxiaChemiSEM (Thermo Fisher Scientific, USA).

Initial State						
Point	**Mn (at.%)**	**Si (at.%)**	**O (at.%)**	**Mn (wt.%)**	**Si (wt.%)**	**O (wt.%)**
1	11.7	9.5	78.8	29.6	12.3	58.1
2	29.7	9.5	60.8	56.8	9.3	33.9
3	22.0	9.1	68.9	47.0	10.0	43.0
4	1.4	25.2	73.4	3.9	36.1	60.0
5	7.0	18.0	75.0	18.3	24.2	57.5
6	17.1	14.7	68.2	38.4	16.9	44.7
7	20.4	5.9	73.7	45.5	6.7	47.8
Sintered at 1100 °C						
Point	**Mn (at.%)**	**Si (at.%)**	**O (at.%)**	**Mn (wt.%)**	**Si (wt.%)**	**O (wt.%)**
1	18.6	14.7	66.7	40.8	16.5	42.7
2	27.3	13.6	59.1	53.1	13.5	33.4
3	16.1	13.2	70.7	37	15.6	47.4
4	18.9	9.9	71.2	42.3	11.3	46.4
5	16.5	16.3	67.2	37.1	18.8	44.1
6	25.7	8.1	66.2	52.3	8.4	39.3
7	27.1	9.2	63.7	53.8	9.4	36.8
8	24.5	20	55.5	48.1	20.1	31.8
9	7.5	19.7	72.8	19.2	26	54.8
10	13	15.5	71.5	31.1	19	49.9

Figure 10 displays micrographs of Bogach ore samples in their initial state and after sintering at 900 °C and 1200 °C. The primary elements detected were Mn, Si, Ca and O. In Figure 10, Mn is represented in purple, Si is depicted in yellow, and Ca is green.

The micrograph at 1000× magnification (Figure 10a) depicts manganese ore with a granular structure composed of spherical and irregularly shaped particles. The particles exhibit a range of sizes, with larger roundish granules mixed with smaller irregular fragments. The surface of the particles appears rough and non-uniform, indicative of natural ore characteristics and potential processing effects. The results of XRD showed the predominance of Mn-containing phases like cryptomelane and braunite. Elemental mapping was performed using EDS to visualize the elemental distribution, with manganese highlighted in purple. The predominance of purple coloring confirms a high manganese content throughout the sample, consistent with its elemental composition and expected phases. The granular morphology and the observed distribution suggest the presence of manganese-rich phases, likely braunite and cryptomelane as the major components. The rough surface textures also hint at possible microstructural heterogeneities within the sample.

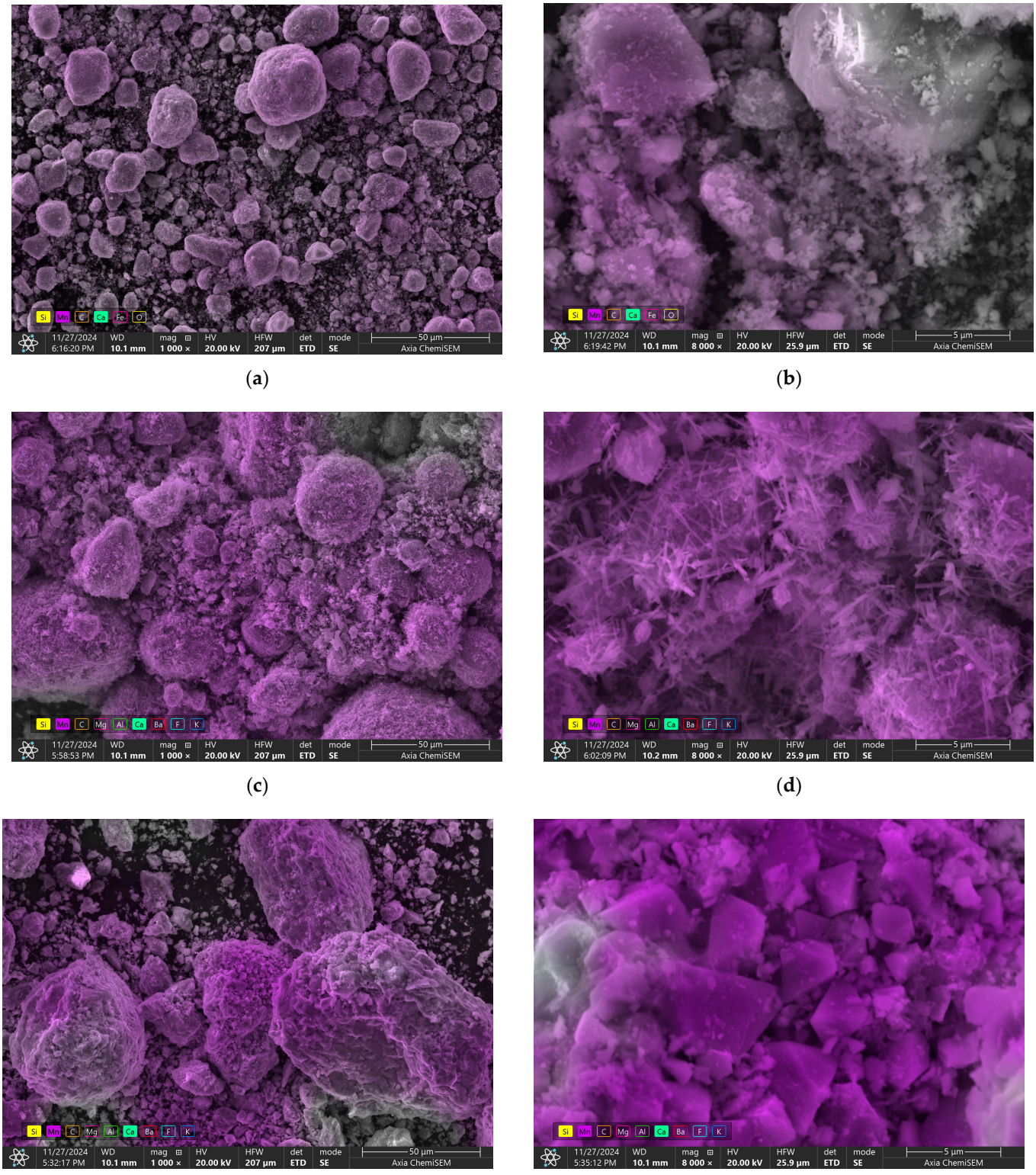

Figure 10. Micrographs of Bogach ore samples: (**a**) in initial state (×1000); (**b**) in initial state (×8000); (**c**) after sintering at 900 °C (×1000); (**d**) after sintering at 900 °C (×8000); (**e**) after sintering at 1200 °C (×1000); and (**f**) after sintering at 1200 °C (×8000). Mn atoms highlighted in purple, Si atoms highlighted in yellow, and Ca atoms highlighted in green.

On the micrograph, at a magnification of ×8000, the structure appears densely packed, with particles showing irregular, non-uniform shapes and sizes (Figure 10b). The manganese-rich regions, highlighted in purple through elemental mapping, show an uneven distribution across the sample. The individual particles are compact, with limited porosity, suggesting that the sample has undergone minimal physical alteration during preparation. The granular texture shows minor flake-like features, which could be a result of mechanical crushing during sample preparation. Silicon-based regions are less pronounced. Overall, the microstructure of this sample demonstrates the significant difference in sizes of particles, which can be explained with the handy sample preparation and significant variety in phase content. Notably, that the surface structure of Bogach ore is loose in contrast to the dense surface of Zhaksy ore sample in the initial state.

Figure 10c illustrates manganese ore after sintering at 900 °C, magnified at ×1000. The structure consists of a variety of particle sizes, predominantly rounded and densely packed grains. These grains exhibit a rough and textured surface characteristic of the thermal transformations during sintering, such as particle coalescence and partial fusion. The image reveals significant agglomeration, forming clusters of manganese-rich regions, which are indicative of enhanced crystallization and phase changes at this temperature.

Although the overall structure appears dense, smaller voids and gaps between particles are noticeable. These voids likely result from incomplete densification or gas release during the sintering process. Additionally, some distinct features such as nanosized rod- or needle-like formations can be observed, suggesting specific crystalline growth patterns triggered under these thermal conditions. The color distribution emphasizes the dominance of manganese throughout the structure, reflecting the compositional and structural evolution of the ore during sintering.

The micrograph, magnified at ×8000, shows a manganese-rich surface highlighted in purple (Figure 10d). The structure is characterized by rod-like and needle-like formations, indicative of crystalline growth patterns. These intricate and elongated structures suggest specific crystallization occurring during sintering at high temperatures. The surface is densely packed with these formations, creating a complex, porous texture. This morphology indicates significant structural transformation, with a high degree of surface roughness and interconnection between the grains.

The micrograph of manganese ore after sintering at 1200 °C, magnified ×1000 (Figure 10e), reveals an increase in grain size due to the high sintering temperature. The surface structure appears rough and complex, with well-defined, large particles that indicate significant coalescence and fusion. The edges and surfaces of the grains seem irregular, suggesting recrystallization and phase growth. The porosity appears minimized, likely due to the high degree of particle bonding. This structural transformation reflects enhanced densification and crystallization typical of elevated sintering temperatures.

The micrograph Figure 10f shows manganese ore sintered at 1200 °C, with a magnification of ×8000. The surface structure reveals the formation of tetragonal crystal structures, indicative of the hausmannite phase. These distinct crystalline forms suggest significant crystallization during the sintering process. The grains are well defined and larger, reflecting increased coalescence and densification at this temperature. The overall texture is rough and complex, with fewer voids, indicating strong particle bonding and a high degree of structural transformation.

Thus, in the initial state, the micrograph of Bogach manganese ore shows a mix of smaller, rounded particles with a rough texture. After sintering at 900 °C, the structure becomes denser with the formation of elongated, needle-like crystals, suggesting phase transitions and increased crystallization. At 1200 °C, the surface reveals more pronounced and larger tetragonal crystals, indicative of significant grain growth and further densification.

The structural transformation reflects enhanced crystallization and phase development at higher temperatures.

Different locations on the micrographs of Bogach ore samples, in their initial state and after sintering at 900 and 1200 °C, were analyzed using point EDS elemental analysis. Figure 11 illustrates the specific locations where spectra were collected, and the corresponding results of the elemental analysis are summarized in Table 7. The analysis was focused on the primary elements present in the samples—Mn, Ca, Si, Fe, C, and O.

Based on the EDS analysis data from Table 7, the Bogach manganese ore samples show distinct compositional variations across different states and sintering temperatures. In the initial state, the samples contain varied amounts of manganese (11.9–65.9 at.%), calcium (0.6–23.1 at.%), and silicon (0.3–2.9 at.%), suggesting the presence of multiple mineral phases. The high manganese content points at 6 and 7 (53.1 and 65.9 at.%) indicate manganese-rich phases, while elevated calcium content at point 4 (23.1 at.%) suggests calcium-rich minerals. The significant oxygen content (17–64.1 at.%) confirms the presence of oxide phases. After sintering at 900 °C, the manganese distribution becomes more uniform (19.3–36.4 at.%), with moderate calcium content (1.5–5.9 at.%). The oxygen levels remain substantial but show less variation compared to the initial state. This suggests phase homogenization during thermal treatment. At 1200 °C, further phase transformation is evident. Manganese content shows increased concentration in several points (up to 42.2 at.%), while calcium content generally decreases, except for point 5 (6.4 at.%). The oxygen content remains significant but shows less variation, indicating the formation of stable oxide phases. The relatively low silicon content across all temperatures suggests that it plays a minor role in the phase composition. The presence of carbon and iron in small quantities might indicate carbonate phases and iron oxide impurities, respectively. These compositional changes reflect the formation of new crystalline phases and increased homogenization at higher sintering temperatures.

Micrographs of Bogach ore after sintering at 900 °C and 1200 °C, as well as Zhaksy ore after sintering at 1100 °C, were analyzed to study particle size distribution. Figure 12 illustrates the features considered for statistical analysis. The results of particle size distribution studies are summarized in Table 8.

Table 7. Elemental content in samples of Bogach ore analyzed via EDS using AxiaChemiSEM (Thermo Fisher Scientific, USA).

	Initial State											
Point	**Mn (at.%)**	**Ca (at.%)**	**Si (at.%)**	**Fe (at.%)**	**C (at.%)**	**O (at.%)**	**Mn (wt.%)**	**Ca (wt.%)**	**Si (wt.%)**	**Fe (wt.%)**	**C (wt.%)**	**O (wt.%)**
1	19.5	1.1	1.4	0	22.4	55.6	46.4	1.9	1.7	0	11.6	38.4
2	20.2	1.2	0.8	0.2	16.3	61.3	46.8	2	0.9	0.4	8.3	41.6
3	14.8	0.6	1.8	0.1	18.6	64.1	38	1	2.4	0.2	10.4	48
4	11.9	23.1	0.3	0.4	10.5	53.8	25.1	35.5	0.4	0.9	4.9	33.2
5	20.4	3.6	2.9	0.4	12.3	60.4	45.1	5.8	3.2	0.9	6	39
6	53.1	2.9	1.2	1.2	13.4	28.2	77.9	3.1	0.9	1.8	4.3	12
7	65.9	8.7	1	1.2	6.2	17	82.1	7.9	0.6	1.5	1.7	6.2
8	12.3	10	1.1	0.2	13.6	62.8	29.6	17.6	1.4	0.6	7.1	43.7
9	16.5	1.2	1.9	0.1	17.6	62.7	40.7	2.2	2.4	0.2	9.5	45
10	17.8	1	1	0.1	17.2	62.9	43.3	1.7	1.3	0.2	9.1	44.4

Table 7. *Cont.*

Initial State												
Point	**Mn (at.%)**	**Ca (at.%)**	**Si (at.%)**	**Fe (at.%)**	**C (at.%)**	**O (at.%)**	**Mn (wt.%)**	**Ca (wt.%)**	**Si (wt.%)**	**Fe (wt.%)**	**C (wt.%)**	**O (wt.%)**
Sintered at 900 °C												
Point	**Mn (at.%)**	**Ca (at.%)**	**Si (at.%)**	**Fe (at.%)**	**C (at.%)**	**O (at.%)**	**Mn (wt.%)**	**Ca (wt.%)**	**Si (wt.%)**	**Fe (wt.%)**	**C (wt.%)**	**O (wt.%)**
1	26.8	5.4	1.1	0.1	14.6	52	53.8	7.9	1.1	0.2	6.4	30.6
2	31.4	5.9	1.7	0.1	13.2	47.7	58.7	8.1	1.6	0.2	5.4	26
3	36.4	3.7	1.4	0.2	10	48.3	64.6	4.8	1.3	0.4	3.9	25
4	24	1.5	3.6	0.3	14.4	56.2	51.2	2.4	4	0.6	6.8	35
5	21.7	2.4	1.2	0.4	17.8	56.5	48.5	3.9	1.4	0.8	8.7	36.7
6	22.4	3	1.2	0.3	15.7	57.4	49	4.9	1.4	0.6	7.5	36.6
7	19.3	2.2	3.4	0.2	16.9	58	44.5	3.7	4.1	0.4	8.5	38.8
8	29.9	1.5	0.8	0.1	14.2	53.5	59.5	2.2	0.8	0.2	6.2	31.1
9	24.7	5.3	1.7	0.2	14.3	53.8	51.1	7.9	1.8	0.3	6.5	32.4
10	33.5	1.9	0.9	0.1	12.3	51.3	63.2	2.5	0.8	0.3	5.1	28.1
Sintered at 1200 °C												
Point	**Mn (at.%)**	**Ca (at.%)**	**Si (at.%)**	**Fe (at.%)**	**C (at.%)**	**O (at.%)**	**Mn (wt.%)**	**Ca (wt.%)**	**Si (wt.%)**	**Fe (wt.%)**	**C (wt.%)**	**O (wt.%)**
1	28.6	0.6	0.6	0.6	14.7	54.9	58.2	0.9	0.6	1.3	6.5	32.5
2	29.3	2.8	2.8	0.3	12.7	52.1	57.5	3.9	2.8	0.6	5.4	29.8
3	38.7	0.7	0.8	0.4	11.1	48.3	68.6	0.9	0.7	0.6	4.3	24.9
4	37.3	0.6	0.6	0.4	9.9	51.2	67.1	0.8	0.6	0.7	3.9	26.9
5	13.8	6.4	4.7	0.1	14.1	60.9	33	11.1	5.7	0.2	7.4	42.6
6	42.2	0.2	0.7	0.5	8.9	47.5	71.5	0.3	0.6	0.9	3.3	23.4
7	34.6	1.6	2	0.4	10.8	50.6	63.9	2.1	1.9	0.7	4.3	27.1
8	22.4	0.6	1.1	0.2	17.3	58.4	50.5	1	1.3	0.4	8.5	38.3

In Bogach ore sintered at 900 °C, a significant number of particles exhibited nano-rod morphology, characterized by their elongated shape with cross-sections averaging 181 nm. After sintering at 1200 °C, the morphology shifts significantly. The particles transition into flake-like structures and agglomerates of these flakes, accompanied by the emergence of a significant number of tetragonal crystalline formations. These formations suggest more pronounced crystal growth and structural reorganization due to the higher temperature.

In Zhaksy sintered at 1100 °C, the particle morphology includes tetragonal-like crystalline formations and roundish particles. This indicates a mix of crystalline growth with a different nature.

In this study, the coefficient of variation (CV) was used to assess the uniformity of particle size distribution by calculating the ratio of standard deviation to mean value, expressed as a percentage. Values below 10% indicated high uniformity in particle sizes, values between 10 and 30% suggested moderate uniformity, and values above 30% reflected high variability in the distribution.

The particle size distributions, as shown in Table 8, vary depending on the sintering temperature and the ore type. In Bogach sintered at 900 °C, the particle sizes are highly variable, with cross-sections of nanorods averaging 181 nm and a wide range from 86 nm to 342 nm. When Bogach is sintered at 1200 °C, the size distribution changes significantly. Flake-like particles exhibit a moderately uniform distribution, while agglomerates and tetragonal crystalline formations are more variable, with the latter showing the greatest variability and larger sizes.

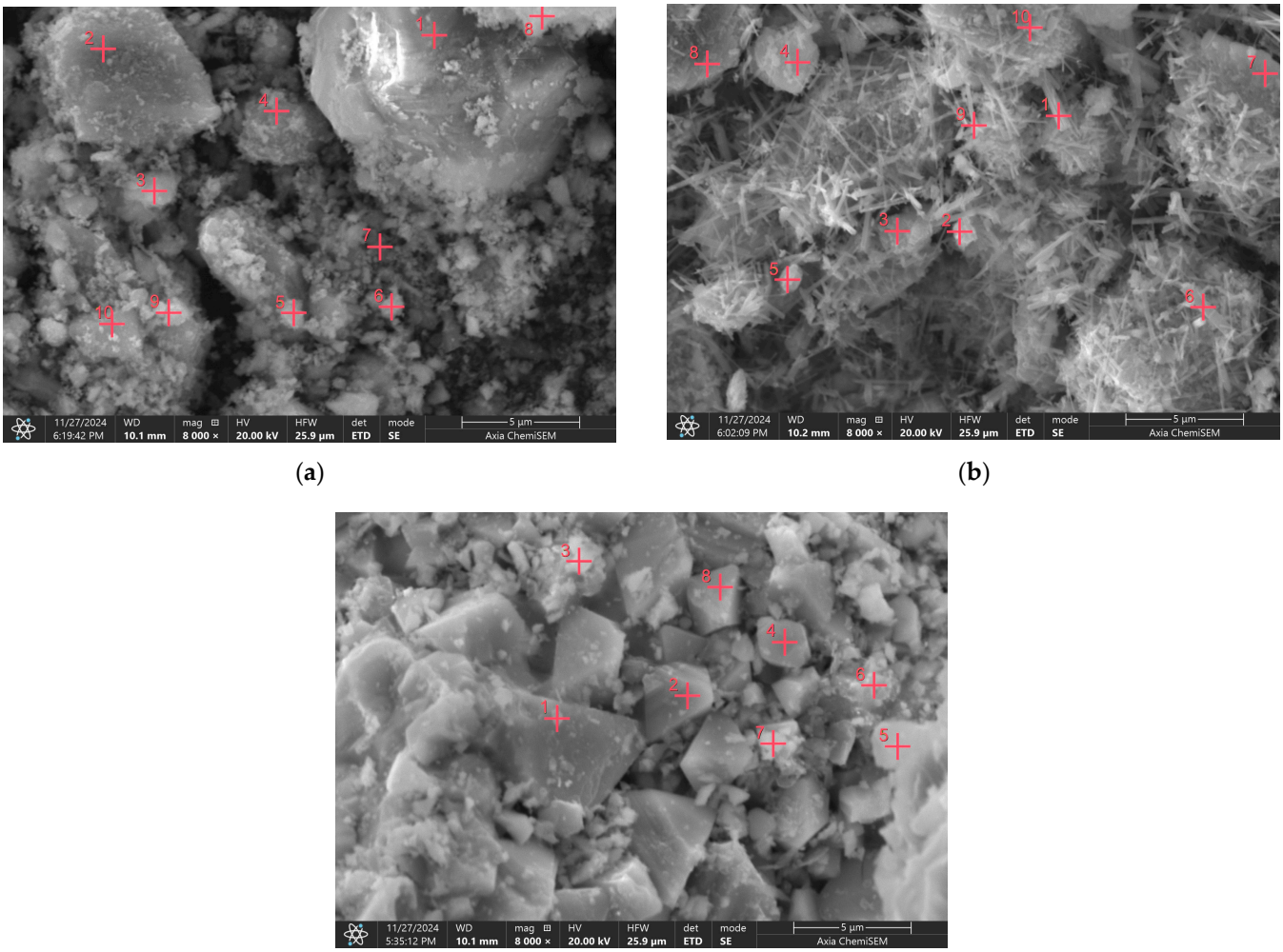

(**a**) (**b**)

(**c**)

Figure 11. Micrographs of Bogach ore sample in initial state (**a**), after sintering at 900 °C (**b**), and after sintering at 1200 °C (**c**) with points for EDS.

In Zhaksy, sintered at 1100 °C, the tetragonal-like crystalline formations and roundish particles display moderately uniform size distributions. The tetragonal-like particles are larger on average than the roundish ones, but both exhibit narrower ranges compared to the highly variable crystalline formations in Bogach.

3.4. Optical Micrographs of the Studied Samples

Figure 13 displays the optical micrographs of the studied manganese ore samples in their initial state and after the sintering processes.

The optical micrographs reveal characteristic transformations in both Bogach and Zhaksy manganese ores during thermal treatment. Bogach ore initially displays dark brownish coloration, appearing notably darker than Zhaksy ore, which suggests higher manganese content. The particle distribution is initially uniform in both ores. As the sintering temperature increases, Bogach ore undergoes a gradual color transition, developing a grayish brown shade at 800 °C, followed by the emergence of distinct bright brownish regions within a grayish brown matrix at 1000 °C. A dramatic change occurs at 1100 °C, where the ore develops brownish black tones with bright reflective spots, attributed to glassy phase formation and recrystallization processes. The sintering above 1000 °C induces melting and vitrification, creating smoother, denser surfaces with enhanced light

reflection. Notably, blackish phases overlay the brown formations observed after 1000 °C treatment, and large agglomerates form at these elevated temperatures.

The Zhaksy ore demonstrates different transformation patterns, transitioning from its initial dark brownish color to increasingly pronounced grayish tones. At 1000 °C, the color becomes notably darker with visible luster, and at 1100 °C, the ore develops a distinctive gray-black shade with increased surface reflectivity. The more pronounced luster in Zhaksy ore compared to Bogach correlates with its higher quartz content and subsequent amorphization. Unlike Bogach, Zhaksy ore does not develop distinct brownish formations during sintering. These variations in color and morphological changes reflect the fundamental differences in mineralogical composition and phase transformations in the studied ores during thermal processing.

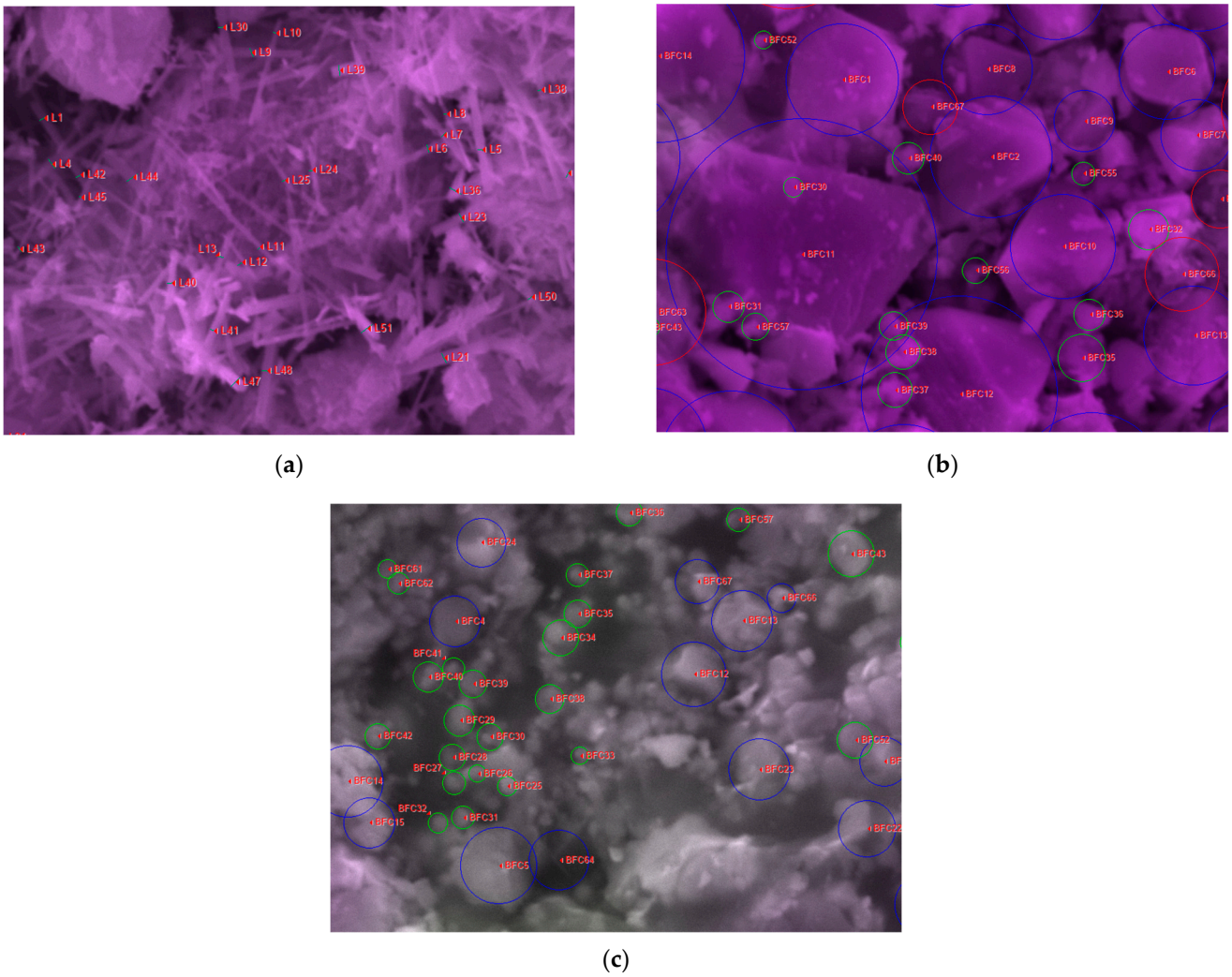

(**a**) (**b**)

(**c**)

Figure 12. Micrographs of studied ore samples with particles selected for size measurements: (**a**) nanorods in Bogach ore sample after sintering at 900 °C; (**b**) tetragonal crystalline formations (blue circles), flake-like particles (green circles), and agglomerates of flake-like particles (red circles) in Bogach ore sample after sintering at 1200 °C; (**c**) tetragonal-like crystalline formations (blue circles), and roundish particles in Zhaksy ore sample after sintering at 1100 °C.

Table 8. Particle morphology and size distribution of Bogach and Zhaksy manganese ores after sintering at different temperatures.

Ore	Bogach (Sintered at 900 °C)	Bogach (Sintered at 1200 °C)			Zhaksy (Sintered at 1100 °C)	
Particle morphology	Nanorods	Flake-like particles	Agglomerates of flake-like particles	Tetragonal crystalline formations	Tetragonal-like crystalline formations	Roundish particles
Type and unit of measurement,	Cross-section of nanorods, nm	Particle diameter, μm	Particle diameter, μm	Particle diameter, μm	Particle diameter, μm	Particle diameter, μm
Number of measured elements	56	30	12	29	29	38
Mean value	181	0.698	2.491	2.923	1.353	0.643
Standard Deviation	55.3	0.169	0.812	1.145	0.368	0.158
Coefficient of Variation (CV)	30.5%	24.2%	32.6%	39.2%	27.2%	24.6%
Interpretation of variability	Highly variable	Moderately uniform	Highly variable	Highly variable	Moderately uniform	Moderately uniform
Minimum	86	0.467	1.427	1.302	0.721	0.441
Maximum	342	1.243	4.023	6.991	2.669	1.156
Range	256	0.776	2.596	5.689	1.948	0.715

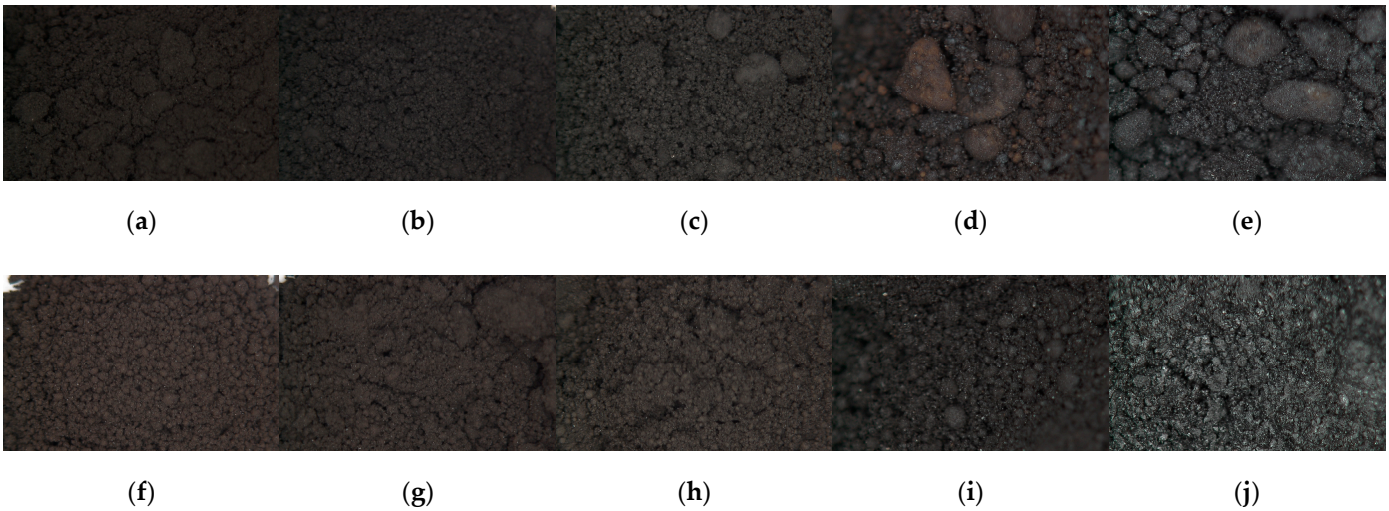

(**a**) (**b**) (**c**) (**d**) (**e**)

(**f**) (**g**) (**h**) (**i**) (**j**)

Figure 13. Optical micrographs of the studied manganese ore samples: from Bogach deposit in initial state (×100) (**a**) and after sintering at 600 °C (×100) (**b**), 800 °C (×100) (**c**), 1000 °C (×200) (**d**), 1100 °C (×200) (**e**); from Zhaksy deposit in initial state (×100) (**f**) and after sintering at 600 °C (×100) (**g**), 800 °C (×100) (**h**), 1000 °C (×200) (**i**), and 1100 °C (×200) (**j**).

Figure 14 displays linear and logarithmic histograms of pixel intensity distribution on optical micrographs of the studied manganese ore samples. The use of a histogram in the logarithmic scale allows a better visualization of details in areas with low signal intensity. This is particularly useful when data have a large dynamic range or when it is necessary to emphasize details in dark areas of the image. The logarithmic scale "compresses" high values and "stretches" low values, making the distribution more visible for analysis.

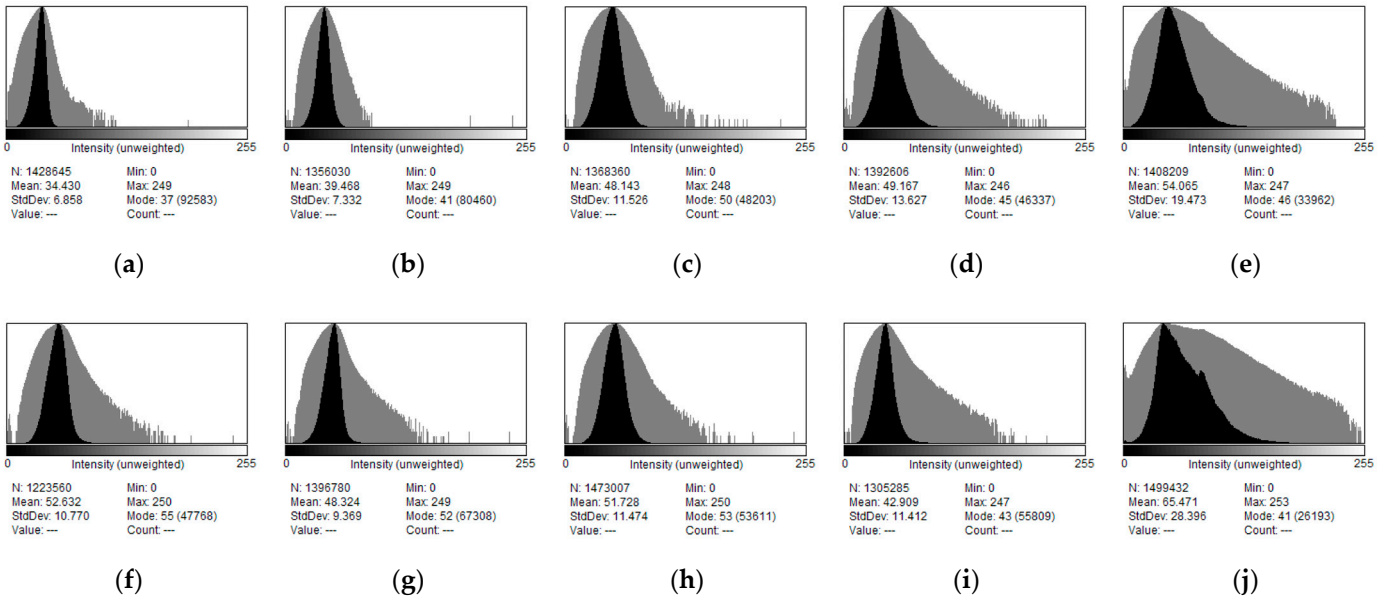

Figure 14. Linear (black) and logarithmic (gray) histograms of pixel intensity distribution (in scale from 0 to 255) on optical micrographs of the studied manganese ore samples: from Bogach deposit in initial state (×100) (**a**) and after sintering at 600 °C (×100) (**b**), 800 °C (×100) (**c**), 1000 °C (×200) (**d**), and 1100 °C (×200) (**e**); from Zhaksy deposit in initial state (×100) (**f**) and after sintering at 600 °C (×100) (**g**), 800 °C (×100) (**h**), 1000 °C (×200) (**i**), and 1100 °C (×200) (**j**).

The histograms in Figure 14 reveal distinct changes in pixel intensity distribution for both Bogach and Zhaksy ores during the sintering process. For Bogach ore (Figure 14a–e), the initial state shows a relatively narrow intensity distribution with a mean value of 34.430. As the sintering temperature increases, the mean intensity gradually rises, reaching 54.065 at 1100 °C, indicating the overall lightening of the sample. The standard deviation also increases from 6.858 to 19.473, suggesting greater variation in brightness and contrast. The logarithmic representation (gray area) shows enhanced detail in low-intensity regions, particularly evident in samples sintered at higher temperatures.

For Zhaksy ore (Figure 14f–j), the initial state shows a higher mean intensity of 52.632 compared to Bogach, confirming its lighter initial appearance. Through the sintering process, the mean intensity fluctuates, ultimately reaching 55.471 at 1100 °C, with a notably high standard deviation of 28.396. The logarithmic histograms reveal a broader distribution of dark tones, particularly pronounced at 1100 °C, indicating more complex surface features and greater variation in brightness. This correlates with the observed increased reflectivity and surface structural changes in the optical micrographs, particularly evident in the formation of glassy phases at higher temperatures.

4. Discussion

4.1. Obtained Phases

The sintering of manganese ores from the Bogach and Zhaksy deposits revealed distinct thermal behaviors, yielding two stable phases: hausmannite (Mn_3O_4) in Bogach ore and braunite ($Mn_2^{+}Mn_6^{3+}SiO_4$) in Zhaksy ore. For Bogach ore, hausmannite became the dominant crystalline phase at 1100 °C and 1200 °C, constituting 90.45 and 95.77 wt.%, respectively. This transformation aligns with prior studies, where hausmannite originates through the thermal decomposition of manganese (III) oxide in air between 950 °C and 1100 °C [50,51]. The phase crystallized as tetragonal structures, characterized by minimal lattice strain and average crystallite sizes of 113.4 nm at 1200 °C. The crystallographic characteristics of hausmannite, including its tetragonal symmetry (space group

I41/amd) and lattice parameters (a = 5.763 Å, c = 9.439 Å), were in agreement with published data [52–54]. The hausmannite crystals exhibited tetrahedral-like morphologies, as observed in SEM micrographs.

The synthesized hausmannite exhibited tetrahedral-like forms, consistent with previous findings. For instance, in [36], hausmannite tetrahedral nanoparticles were derived from West Sumatera manganese ore, showing that the sintering process influences phase formation. The hausmannite phase emerged at 700 °C, and sintering temperature variations facilitated its formation. Similarly, [30] reported manganese powders synthesized via dry precipitation from natural manganese ore, where sintering temperature impacted the crystal structure and grain size of manganese oxide. Higher sintering temperatures caused structural changes and increased grain size in the hausmannite phase. As well, in [33], Mn_3O_4 was synthesized as nano-octahedral crystals using a hydrothermal method with polyethylene glycol (PEG200) serving as a reductant and shape-directing agent. Micrographs of synthesized hausmannite were presented in which the shapes of crystals were quite similar to those obtained in this study.

Notably, at intermediate sintering temperatures (900 °C), nanorod-like formations appeared, likely representing transitional structures. These nanorods could correspond to metastable hydromanganite or MnO(OH) phases, as previously reported in analogous studies [32,33]. However, no definitive evidence of MnO(OH) phases was detectable in this study due to the complexity of natural ore compositions.

In Zhaksy ore, braunite emerged as the predominant crystalline phase after sintering at 1100 °C (83.81 wt.%). The crystallized braunite displayed tetragonal morphology, consistent with its reported crystallographic parameters. Braunite formation dominated the sintering process, with crystallographic parameters (a = 9.432 Å, c = 18.703 Å) consistent with previously reported values [55]. Published literature describes braunite as forming polyhedral or pseudo-octahedral crystals [56], which align with the well-defined crystal surfaces observed in the micrographs.

4.2. Morphological Evolution

Both ores exhibited significant morphological and color changes during sintering. In Bogach ore, the initial structure of irregular grains evolved into densely packed, elongated needle- and rod-like structures at 900 °C, consistent with recrystallization during intermediate-phase stabilization. At 1200 °C, the grains coalesced into larger, well-defined tetragonal crystals, characteristic of hausmannite. Bogach ore transitioned from a dark brownish shade in its initial state to a brownish black hue at 1200 °C, consistent with the characteristics of hausmannite.

In contrast, Zhaksy ore shifted from brownish gray tones to a distinctive grayish black shade at 1100 °C, reflecting enhanced braunite crystallization and quartz amorphization. SEM micrographs revealed that the increase in sintering temperature promoted particle coalescence, grain growth, and surface smoothing. The development of surface gloss above 1100 °C was more pronounced in Zhaksy ore, correlating with its higher quartz content. This gloss can be attributed to surface vitrification or partial melting of quartz and other amorphous components.

Upon heating a polymineral rock, the phase with the lowest melting point begins to melt first. As the temperature increases, this low-temperature phase melt reacts with the surface layers of higher-melting-point phases. This interaction results in the formation of melts with intermediate chemical compositions, giving the melt a zonal structure [57]. Research indicates that the surface melting temperature of crystals in various compounds is approximately 50–87% of their bulk melting temperatures [58]. In addition, the degree of sample grinding during preparation plays a significant role. The complete melting of a

polymineral rock sample typically occurs at a temperature much higher than the melting point of the finely ground powder of the same sample.

Given the grinding of the samples during preparation and the fact that melting zones are primarily surface phenomena without forming a bulk melt, it is reasonable to conclude that quartz may undergo surface amorphization. In other words, although quartz has a high bulk melting point (1720 °C [59]), surface melting or amorphization can occur at significantly lower temperatures, particularly as a surface melting process for fine powders. Moreover, quartz can interact with other amorphous or dispersed phases acting as fluxes. The amorphized substances interact with the surfaces of high-temperature phases, forming a characteristic amorphous coating, as clearly observed in Figures 8e and 10e. Moreover, not only quartz but also other less thermally stable components, which might be part of the amorphous phase but undetected via diffraction methods, may undergo surface melting. Importantly, the appearance of smooth surfaces and luster is more pronounced in the Zhaksy ore, which contains notably higher quartz content. This finding establishes a direct correlation between the quartz content and the ability of the ore to form surface melts during sintering.

Therefore, the crystallization of the ore surface due to sintering is reflected in changes in both color and texture. Additionally, the results suggest that quartz in the Zhaksy ore either undergoes amorphization or interacts with other components to form a surface melt layer. This melt either amorphizes quartz or obscures the crystalline quartz beneath it. This phenomenon accounts for the reduced intensity of quartz reflections in X-ray diffraction patterns after high-temperature sintering. Conversely, braunite appears to crystallize from amorphous components, leading to the formation of tetragonal-like crystals and accompanying color changes.

4.3. Compositional Changes

It has been determined that the Bogach deposit is characterized by a more pronounced manganese content, whereas the Zhaksy deposit contains a significant amount of silicon. The elemental composition of these deposits is largely determined by their formation processes and mineralogical composition. The Bogach deposit is primarily composed of oxidized manganese minerals such as cryptomelane, braunite, and hollandite. These phases are rich in manganese due to their mineralogical characteristics, where manganese oxides dominate over silicates. In contrast, the Zhaksy deposit contains an abundance of braunite ($3Mn_2O_3 \cdot MnSiO_3$) and quartz (SiO_2) as primary phases. Braunite inherently incorporates significant silicon in its structure, while quartz serves as a major source of silicon content in the deposit.

XRF and EDS analyses demonstrated reduced phase complexity and increased elemental uniformity after sintering. For Bogach ore, manganese content increased (65.7 wt.% at 1100 °C), reflecting the transition from less stable oxides to more reduced hausmannite. Conversely, silicon content diminished, correlating with the loss of quartz reflections in XRD patterns above 900 °C. Similar trends were observed for calcium and aluminum, suggesting their incorporation into minor phases or amorphous components.

The Zhaksy ore displayed a more stable manganese distribution but showed significant reductions in silicon content, from 20.85 wt.% in the initial state to 12.9 wt.% at 1100 °C. This decrease aligns with the amorphization of quartz and other silicon-containing phases. Iron content in Zhaksy ore remained relatively stable, reflecting the persistence of hematite at intermediate temperatures and its disappearance at higher sintering levels. Elemental mappings also showed sharper delineations between manganese- and silicon-rich phases at lower sintering temperatures, which became less pronounced at higher temperatures due to interphase interactions.

4.4. Mechanisms of Sintering

At its core, the sintering process involves diffusion, densification, and phase transformation, enabling the consolidation and transformation of the ore into more stable manganese oxide phases.

As the temperature of the Bogach ore increases during sintering (600–1200 °C), several thermally induced phenomena occur. Initially, the ore contains a mixture of cryptomelane, braunite, and quartz phases. At around 900 °C, significant recrystallization begins, characterized by the formation of nanorod-like structures, indicative of intermediate phases like MnO(OH) or metastable manganese oxides. Quartz peaks diminish, reflecting its progressive transition into an amorphous state. The manganese content increases due to the decomposition of volatile components and less stable phases, resulting in the enhancement of manganese enrichment in the crystalline phase.

At higher temperatures (1000–1200 °C), the transformation into hausmannite (Mn_3O_4) becomes dominant. This phase evolves through a diffusion-driven process where manganese ions migrate, rearrange, and stabilize into a tetragonal structure. By 1200 °C, hausmannite comprises the majority of the crystalline content, as seen in the XRD patterns. The densification process is evident in SEM micrographs, where particles coalesce and form larger, well-defined structures. The surface exhibits tetragonal crystal formations with rough, porous textures attributed to the release of gases during crystallization. The decreased quartz reflections further confirm the significant reduction in silicon-containing phases, correlating with the dominance of manganese-rich oxides.

The sintering process for Bogach ore demonstrates a clear sequence of transformations: (1) initial recrystallization of manganese oxides, (2) densification and growth of hausmannite crystals, and (3) progressive reduction in silicon phases through amorphization. These mechanisms lead to a final structure with enhanced manganese content and optimal phase composition, suitable for industrial applications such as catalysts and pigments.

The sintering mechanism of the Zhaksy ore is characterized by diffusion, densification, and phase transformations that involve the manganese silicate phase braunite (Mn_7SiO_{12}) and significant changes in quartz (SiO_2). Initially, at lower sintering temperatures, the ore exhibits a high amorphous content, with crystalline components dominated by quartz and braunite. As the temperature increases, diffusion processes become more active, enabling the rearrangement of atoms and the growth of braunite crystals. Around 900 °C, microstructural and phase transformations become evident. Braunite starts to crystallize more prominently, while quartz begins to amorphize, as shown by decreasing quartz peak intensity in XRD patterns.

At 1100 °C, braunite becomes the dominant phase, comprising up to 83.81% of the crystalline content, as quartz undergoes further amorphization and disappears from the diffraction patterns. This increased braunite crystallization reflects the enhanced mobility of manganese and silicon, which diffuse and reorganize to stabilize this manganese silicate phase. SEM micrographs reveal a porous, granular structure with interconnected manganese-rich particles. The interconnected granules suggest partial densification, though some residual porosity remains.

The overall sintering behavior of the Zhaksy ore is strongly influenced by its mineral composition, particularly the coexistence of braunite and quartz. The interaction between these phases during thermal treatment enhances braunite crystallization and reduces silicon segregation.

4.5. Limitations and Future Directions

The primary limitation of this study lies in the fact that some transitional phases, such as MnOOH, may not have been fully identified due to the complexity of the ore

composition and the limitations of the analysis techniques. Future work should focus on employing complementary methods, such as Raman spectroscopy, to better resolve these phases. Moreover, the role of amorphous components in influencing phase transitions and surface vitrification warrants further exploration. Advanced characterization techniques, such as Raman spectroscopy or transmission electron microscopy (TEM), could provide further insights into these phases. The mechanical and catalytic properties of the obtained hausmannite and braunite products should also be investigated to assess their potential industrial applications.

5. Conclusions

This study comprehensively evaluated the phase transitions, structural evolution, and compositional changes of manganese ores from the Bogach and Zhaksy deposits following heat treatments at various sintering temperatures. Through the combination of XRD, SEM, and elemental analyses, the thermal behavior of these ores under high-temperature conditions was elucidated. The findings not only provide valuable insights into phase transformations but also open new possibilities for the practical application of these materials in producing high-value manganese oxide products. The following main results were obtained:

1. Heat treatment of Bogach and Zhaksy manganese ores led to the formation of thermally stable manganese oxide phases. For Bogach ore, hausmannite (Mn_3O_4) became the dominant phase after sintering at 1000 °C, eventually reaching 95.77 wt.% at 1200 °C. In Zhaksy ore, braunite ($Mn_7O_{12}Si$) was the primary crystalline phase, with its share peaking at 83.81 wt.% after sintering at 1100 °C.
2. Both ores showed reductions in crystalline quartz content with an increasing temperature. In Zhaksy ore, quartz underwent significant amorphization above 900 °C, decreasing from 64.85 wt.% in the initial state to 16.19 wt.% at 1100 °C. This aligns with the structural changes observed in micrographs, where amorphous regions became more pronounced.
3. SEM micrographs revealed significant structural transformations during sintering. For Bogach ore, needle-like and rod-like formations were observed at 900 °C, evolving into well-defined tetragonal crystals at 1200 °C. In Zhaksy ore, the transition to smoother, denser structures with more pronounced crystalline formations was notable at 1100 °C.
4. XRF and EDS analyses showed temperature-dependent changes in elemental distribution. In Bogach ore, manganese content increased from 60.77 wt.% in the initial state to 65.7 wt.% at 1100 °C, indicating phase homogenization. In Zhaksy ore, manganese content remained relatively stable, but silicon content decreased significantly from 20.85 wt.% at 25 °C to 12.90 wt.% at 1100 °C, correlating with quartz amorphization.
5. The presence of smooth surfaces and surface luster, particularly in Zhaksy ore, confirmed a correlation between high quartz content and surface melting. The partial amorphization of quartz influenced the structural and optical properties of the sintered materials, contributing to the overall changes in morphology and light reflectivity.

The findings of this study have practical relevance for the extraction and utilization of medium-grade manganese ores in Central Kazakhstan. The successful synthesis of hausmannite and braunite, which have applications as catalysts and pigments, and in the production of construction materials, highlights the potential for developing cost-effective technologies to produce high-value products from local raw materials. This approach addresses the challenge of diminishing high-grade manganese reserves by focusing on underutilized medium-grade ores, thereby reducing raw material waste and promoting

sustainable resource management. The techniques and temperature regimes presented here provide a foundation for optimizing sintering processes in industrial applications.

The findings have broader implications for the manganese ore processing industry, especially in regions with similar medium-grade deposits. By utilizing local raw materials and applying cost-effective sintering technologies, it is possible to create competitive, high-value products with a minimal environmental impact. This approach not only supports regional economic development but also contributes to the global shift toward more sustainable practices in mineral processing. These efforts align with the growing demand for eco-friendly technologies and resource-efficient manufacturing processes.

Author Contributions: Conceptualization, R.Z.S.; methodology, R.Z.S., J.B.K. and L.D.L.S.V.; software, A.K.Z., J.B.K. and H.S.C.; validation, C.H.W.B. and L.D.L.S.V.; formal analysis, E.E.K. and R.M.K.; investigation, Y.A.B., A.K.Z. and H.S.C.; resources, Y.A.B. and R.M.K.; data curation, R.Z.S.; writing—original draft, Y.A.B., A.K.Z. and H.S.C.; writing—review and editing, R.Z.S. and L.D.L.S.V.; visualization, E.E.K. and L.D.L.S.V.; supervision, C.H.W.B.; project administration, R.Z.S.; funding acquisition, R.Z.S. All authors have read and agreed to the published version of the manuscript.

Funding: The given research was carried out within the framework of a project funded by the Science Committee of the Ministry of Science and Higher Education of the Republic of Kazakhstan (Grant No. AP23488858).

Data Availability Statement: The original contributions presented in this study are included in the article. Further inquiries can be directed to the corresponding authors.

Acknowledgments: The experimental works were partly performed at Cavendish Laboratory, Cambridge University (Cambridge, UK), during the scientific internship "500 scientists" by the Ministry of Science and Higher Education of the Republic of Kazakhstan. H. Sanchez Cornejo thanks the Peruvian Agency CONCYTEC for financial support through grant No.PE501083676-2023-PROCIENCIA.

Conflicts of Interest: The authors declare no conflicts of interest.

References

1. Kozłowska, A.; Grajcar, A.; Opara, J.; Kaczmarczyk, J.; Janik, A.; Radwański, K. Mechanical Behaviour and Micromechanical Modelling of Medium-Mn Steel Microstructure Evolution. *Int. J. Mech. Sci.* **2022**, *220*, 107151. [CrossRef]
2. Liu, X.; Zhao, Y.; Zhou, W.; Yuan, S.; Wang, X. New Progress in the Development and Utilization of Ferromanganese Ore. *Miner. Eng.* **2024**, *216*, 108826. [CrossRef]
3. Singla, Y.K.; Maughan, M.R.; Arora, N.; Dwivedi, D.K. Enhancing the Wear Resistance of Iron-Based Alloys: A Comprehensive Review of Alloying Element Effects. *J. Manuf. Process.* **2024**, *120*, 135–160. [CrossRef]
4. Zhu, E.; Geng, Y.; Xiao, S.; Guo, T.; Gao, Z.; Gao, Z. Mapping the Evolution of Manganese Flows and Stocks in China from 2000 to 2021. *Resour. Environ. Sustain.* **2024**, *16*, 100152. [CrossRef]
5. Pérez, K.; Toro, N.; Robles, P.; Gallegos, S.; Gálvez, E.; González, F.J.; Marino, E.; Hernández, P.C. Cobalt and Manganese Extraction from Ocean Nodules by Co-Processing with Steel Metallurgical Slag. *Metals* **2023**, *13*, 1079. [CrossRef]
6. Ntunka, M.; Loveday, B. Sustainable Production of Electrolytic Manganese Dioxide (EMD): A Conceptual Flowsheet. *Clean. Chem. Eng.* **2025**, *11*, 100145. [CrossRef]
7. Yu, D.; Cui, F.; Cong, Y.; Zhang, C.; Tian, Q.; Guo, X. Simultaneous Selective Chlorination and Carbothermic Reduction of High-Iron Manganese Ore for the Recovery of Manganese Chloride and Metallic Iron. *Metals* **2019**, *9*, 1124. [CrossRef]
8. Xiao, J.; Zou, K.; Chen, T.; Xiong, W.; Deng, B. Extraction of Manganese and Iron from a Refractory Coarse Manganese Concentrate. *Metals* **2021**, *11*, 563. [CrossRef]
9. Zhuniskaliyev, T.; Nurumgaliyev, A.; Zayakin, O.; Mukhambetgaliyev, Y.; Kuatbay, Y.; Mukhambetkaliyev, A. Investigation and Comparison of the Softening Temperature of Manganese Ores Used for the Production of Complex Ligatures Based on Fe-Si-Mn-Al. *Metalurgija* **2020**, *59*, 521–524.
10. Yushko, S.A.; Lazur, Y.M. Mineral Associations of the Zhaksy-Kotr Manganese Deposit (Central Kazakhstan). *Int. Geol. Rev.* **1979**, *21*, 403–407. [CrossRef]
11. Akylbekov, S.A. Manganese of Kazakhstan. *News Natl. Acad. Sci. Repub. Kazakhstan Ser. Geol. Tech. Sci.* **2006**, *1*, 42–53. Available online: http://nblib.library.kz/elib/library.kz/Jurnal/g_2006_1/42-53.pdf (accessed on 15 January 2025). (In Russian).

12. Liu, Y.; He, F.; Ma, D.; Hu, Q.; You, Z. Novel Process of Reduction Roasting Manganese Ore with Sulfur Waste and Extraction of Mn by Acid Leaching. *Metals* **2022**, *12*, 384. [CrossRef]
13. Kies, F.; Wilms, M.B.; Pirch, N.; Pradeep, K.G.; Schleifenbaum, J.H.; Haase, C. Defect Formation and Prevention in Directed Energy Deposition of High-Manganese Steels and the Effect on Mechanical Properties. *Mater. Sci. Eng. A* **2020**, *772*, 138688. [CrossRef]
14. Sosnovskii, L.A.; Baglyuk, G.A.; Vlasova, O.V.; Golovkova, M.E. Structure and Properties of Sintered Silicon–Manganese Steels. *Powder Metall. Met. Ceram.* **2015**, *53*, 657–662. [CrossRef]
15. Gamutan, J.; Miki, T.; Nagasaka, T. Morphology and Composition of Inclusions in Si-Mn Deoxidized Steel at the Solid-Liquid Equilibrium Temperature. *ISIJ Int.* **2020**, *60*, 84–91. [CrossRef]
16. Soltani, H.; Bahiraei, H.; Ghasemi, S.; Hashempour, M. Rate Capability and Electrolyte Concentration: Tuning MnO_2 Supercapacitor Electrodes through Electrodeposition Parameters. *Heliyon* **2025**, *11*, e41427. [CrossRef]
17. Li, P.; Luo, S.-H.; Wang, X.; Wang, L.; Wang, J.; Teng, F.; Wang, Q.; Zhang, Y.; Liu, X.; Zhang, H.; et al. Study on the High-Efficiency Separation of Fe and Mn from Low-Grade Pyrolusite and the Preparation of LiMn2O4 Materials for Lithium-Ion Batteries. *Sep. Purif. Technol.* **2022**, *278*, 119611. [CrossRef]
18. Srivastava, G.; Dalela, S.; Kumar, S.; Choudhary, B.L.; Alvi, P.A. Structural and Raman Studies of MnO_2 and Mn_2O_3 Nano-Particles. *Mater. Today Proc.* **2023**, *79*, 169–171. [CrossRef]
19. Feng, W.; Faraj, Y.; Yan, Y.; An, Y.; Xie, R.; Lai, B. Novel Pyrolusite-Templated Biochar as an Outstanding Catalyst for Persulfate Activation: Structural Design, Synergistic Effect, and Mechanism. *Ind. Eng. Chem. Res.* **2022**, *61*, 1885–1896. [CrossRef]
20. Grifasi, N.; Sartoretti, E.; Montesi, D.; Bensaid, S.; Russo, N.; Deorsola, F.A.; Fino, D.; Novara, C.; Giorgis, F.; Piumetti, M. Mesostructured Manganese Oxides for Efficient Catalytic Oxidation of CO, Ethylene, and Propylene at Mild Temperatures: Insight into the Role of Crystalline Phases and Physico-Chemical Properties. *Appl. Catal. B Environ. Energy* **2025**, *362*, 124696. [CrossRef]
21. Jiang, Y.; Cheng, S.; Su, C.; Jiang, Y.; Sun, X.; Zhang, G.; Liu, Y.; Dou, X.; Yang, Z. Bimetallic Mn-Cu Oxide Catalysts for Toluene Oxidation: Synergistic Effect and Catalytic Mechanism. *Appl. Surf. Sci.* **2024**, *670*, 160629. [CrossRef]
22. Flook, R. Manganese: The Black Art. *Benchmark Miner. Intell.* **2019**, *1*, 38–47.
23. Deraz, N. Green Synthesis, Characterization and Magnetic Properties of Hausmannite Nanoparticles. *Acta Phys. Pol. A* **2019**, *136*, 147–150. [CrossRef]
24. Pligin, E.I.; Lavysh, A.V.; Lugovskii, A.A.; Voropay, E.S.; Kopishev, É.E.; Maskevich, A.A. Luminescence Spectral Properties of New Benzothiazole Polymethine Dye. *J. Appl. Spectrosc.* **2023**, *89*, 1021–1028. [CrossRef]
25. Ahmed, N. Recent Advances and Emerging Opportunities in Mechanism and Applications of Earth Abundant Manganese-Catalysts for Sustainable Organic Transformations. *J. Organomet. Chem.* **2024**, *1009*, 123071. [CrossRef]
26. Chen, S.; Li, H.; Hao, Y.; Chen, R.; Chen, T. Porous Mn-Based Oxides for Complete Ethanol and Toluene Catalytic Oxidation: The Relationship between Structure and Performance. *Catal. Sci. Technol.* **2020**, *10*, 1941–1951. [CrossRef]
27. Pulleri, J.K.; Singh, S.K.; Yearwar, D.; Saravanan, G.; Al-Fatesh, A.S.; Labhasetwar, N.K. Morphology Dependent Catalytic Activity of Mn_3O_4 for Complete Oxidation of Toluene and Carbon Monoxide. *Catal. Lett.* **2021**, *151*, 172–183. [CrossRef]
28. Ali, S.; Iqbal, Y.; Fahad, M. A Comprehensive Phase, Minero-Chemical and Microstructural Investigation of Low-Grade Manganese Ore. *Mater. Res. Express* **2019**, *6*, 115527. [CrossRef]
29. Vodyanitskii, Y.N. Mineralogy and Geochemistry of Manganese: A Review of Publications. *Eurasian Soil Sci.* **2009**, *42*, 1170–1178. [CrossRef]
30. Fauzi, A.; Ratnawulan; Putri, P.J. Effect of Sintering Temperature on Crystal Structure and Grain Size of Manganese Ores from West Sumatera. *J. Phys. Conf. Ser.* **2018**, *1040*, 012051. [CrossRef]
31. Wang, Y.; Hou, C.; Lin, X.; Jiang, H.; Zhang, C.; Liu, G. Dye Degradation Studies of Hausmannite Manganese Oxide (Mn_3O_4) Nanoparticles Synthesized by Chemical Method. *Appl. Phys. A-Mater. Sci. Process.* **2021**, *127*, 277. [CrossRef]
32. Ahmed, K.A.M.; Peng, H.; Wu, K.; Huang, K. Hydrothermal Preparation of Nanostructured Manganese Oxides (MnOx) and Their Electrochemical and Photocatalytic Properties. *Chem. Eng. J.* **2011**, *172*, 531–539. [CrossRef]
33. Li, Y.; Tan, H.; Yang, X.; Goris, B.; Verbeeck, J.; Bals, S.; Colson, P.; Cloots, R.; Van Tendeloo, G.; Su, B. Well Shaped Mn_3O_4 Nano-octahedra with Anomalous Magnetic Behavior and Enhanced Photodecomposition Properties. *Small* **2011**, *7*, 475–483. [CrossRef] [PubMed]
34. Sukhdev, A.; Challa, M.; Narayani, L.; Manjunatha, A.S.; Deepthi, P.R.; Angadi, J.V.; Mohan Kumar, P.; Pasha, M. Synthesis, Phase Transformation, and Morphology of Hausmannite Mn_3O_4 Nanoparticles: Photocatalytic and Antibacterial Investigations. *Heliyon* **2020**, *6*, e03245. [CrossRef] [PubMed]
35. Rani, B.J.; Ravina, M.; Ravi, G.; Ravichandran, S.; Ganesh, V.; Yuvakkumar, R. Synthesis and Characterization of Hausmannite (Mn_3O_4) Nanostructures. *Surf. Interfaces* **2018**, *11*, 28–36. [CrossRef]
36. Ratnawulan; Prasetyo, F.; Fauzi, A. Ramli Synthesis and Characterization Hausmannite (Mn_3O_4) Nanoparticle of Manganese Ores Prepared By High-Energy Milling. *Int. J. Adv. Sci. Technol.* **2020**, *29*, 8332–8339.

37. Reddy, U.M.; Gopalkrishna, S.J.; Kumar, P.S.; Hatti, B. Characterization and Processing of Low Grade Iron Rich Manganese Ore. *Int. J. Sci. Technol. Res.* **2019**, *8*, 2448–2451.
38. Aripin, H.; Priatna, E.; Busaeri, N.; Hiron, N.; Sabchevski, S. Reduction Behavior of Medium Grade Manganese Ore from Karangnunggal during a Sintering Process in Methane Gas. *IOP Conf. Ser. Mater. Sci. Eng.* **2019**, *550*, 012036. [CrossRef]
39. Moradkhani, D.; Malekzadeh, M.; Ahmadi, E. Nanostructured MnO_2 Synthesized via Methane Gas Reduction of Manganese Ore and Hydrothermal Precipitation Methods. *Trans. Nonferrous Met. Soc. China (Engl. Ed.)* **2013**, *23*, 134–139. [CrossRef]
40. Sorensen, B.; Gaal, S.; Tangstad, M.; Ringdalen, E.; Kononov, R.; Ostrovski, O. Properties of Manganese Ores and Their Change in the Process of Calcination. In Proceedings of the Twelfth International Ferroalloys Congress Sustainable Future, Helsinki, Finland, 6–9 June 2010; pp. 439–448.
41. Fujii, Y.; Nakai, Y.; Uchida, Y.-I.; Miki, Y. Fundamental Investigation of High Temperature Reduction and Melting Behavior of Manganese Ore. *ISIJ Int.* **2017**, *57*, 609–614. [CrossRef]
42. Cheraghi, A.; Yoozbashizadeh, H.; Safarian, J. Gaseous Reduction of Manganese Ores: A Review and Theoretical Insight. *Miner. Process. Extr. Metall. Rev.* **2020**, *41*, 198–215. [CrossRef]
43. Anacleto, N.; Ostrovski, O.; Ganguly, S. Reduction of Manganese Ores by Methane-Containing Gas. *ISIJ Int.* **2004**, *44*, 1615–1622. [CrossRef]
44. Chen, J.; Li, L.; Chen, G.; Peng, J.; Srinivasakannan, C. Rapid Thermal Decomposition of Manganese Ore Using Microwave Heating. *J. Alloys Compd.* **2017**, *699*, 430–435. [CrossRef]
45. Dankwah, J.R.; Asamoah, D.N. Utilisation of Post-Consumer Plastics in Pre-Reduction of Higher Manganese Oxides in Ferromanganese Process. *Ironmak. Steelmak.* **2013**, *40*, 138–146. [CrossRef]
46. Sorensen, B.; Gaal, S.; Ringdalen, E.; Tangstad, M.; Kononov, R.; Ostrovski, O. Phase Compositions of Manganese Ores and Their Change in the Process of Calcination. *Int. J. Miner. Process.* **2010**, *94*, 101–110. [CrossRef]
47. Vaitkus, A.; Merkys, A.; Sander, T.; Quirós, M.; Thiessen, P.A.; Bolton, E.E.; Gražulis, S. A Workflow for Deriving Chemical Entities from Crystallographic Data and Its Application to the Crystallography Open Database. *J. Cheminformatics* **2023**, *15*, 123. [CrossRef]
48. Doebelin, N.; Kleeberg, R. Profex: A Graphical User Interface for the Rietveld Refinement Program BGMN. *J. Appl. Crystallogr.* **2015**, *48*, 1573–1580. [CrossRef]
49. ImageJ. Available online: https://imagej.net/ij/index.html (accessed on 6 December 2024).
50. Liu, J.; Baeyens, J.; Deng, Y.; Wang, X.; Zhang, H. High Temperature Mn_2O_3/Mn_3O_4 and Co3O4/CoO Systems for Thermo-Chemical Energy Storage. *J. Environ. Manag.* **2020**, *267*, 110582. [CrossRef] [PubMed]
51. Jacob, K.T.; Kumar, A.; Rajitha, G.; Waseda, Y. Thermodynamic Data for Mn_3O_4, Mn_2O_3 and MnO_2. *High Temp. Mater. Process.* **2011**, *30*, 459–472. [CrossRef]
52. Baron, V. The Influence of Iron Substitution on the Magnetic Properties of Hausmannite, Mn^{2+}(Fe,Mn)23+04. *Am. Mineral.* **1998**, *83*, 786–793. [CrossRef]
53. Durdubaeva, R.; Beknazarov, H.; Asamatdinov, A.; Yusupova, N. Study of Steel Corrosion Inhibition with the Use of Secondary Waste. *Bull. LN Gumilyov Eurasian Natl. Univ. Chem. Geogr. Ecol. Ser.* **2022**, *138*, 31–36. [CrossRef]
54. Hausmannite. Available online: https://www.mindat.org/min-1832.html (accessed on 10 December 2024).
55. Miletich, R.; Allan, D.R.; Angel, R.J. Structural Control of Polyhedral Compression in Synthetic Braunite, Mn 2+ Mn 3+ 6 O 8 SiO 4. *Phys. Chem. Miner.* **1998**, *25*, 183–192. [CrossRef]
56. Braunite. Available online: https://www.mindat.org/min-757.html (accessed on 9 December 2024).
57. Sobolev, R.N.; Maltsev, V.V.; Volkova, E.A. Experimental study of the melting process of minerals and rocks. *Melts* **2020**, *3*, 246–257. [CrossRef]
58. Sobolev, R.N. The Surface Layer of a Crystal and Its Specific Role in the Process of Melt Formation. *Dokl. Earth Sci.* **2018**, *479*, 495–498. [CrossRef]
59. Bestmann, M.; Pennacchioni, G.; Frank, G.; Göken, M.; De Wall, H. Pseudotachylyte in Muscovite-Bearing Quartzite: Coseismic Friction-Induced Melting and Plastic Deformation of Quartz. *J. Struct. Geol.* **2011**, *33*, 169–186. [CrossRef]